

AD _____

Award Number: DAMD17-00-1-0459

TITLE: Non-Invasive Monitoring of Breast Tumor Oxygenation:
A Key to Tumor Therapy Planning and Tumor Prognosis

PRINCIPAL INVESTIGATOR: Hanli Liu, Ph.D.

CONTRACTING ORGANIZATION: The University of Texas at Arlington
Arlington, Texas 76019-0145

REPORT DATE: September 2002

TYPE OF REPORT: Annual

PREPARED FOR: U.S. Army Medical Research and Materiel Command
Fort Detrick, Maryland 21702-5012

DISTRIBUTION STATEMENT: Approved for Public Release;
Distribution Unlimited

The views, opinions and/or findings contained in this report are those of the author(s) and should not be construed as an official Department of the Army position, policy or decision unless so designated by other documentation.

REPORT DOCUMENTATION PAGEForm Approved
OMB No. 074-0188

Public reporting burden for this collection of information is estimated to average 1 hour per response, including the time for reviewing instructions, searching existing data sources, gathering and maintaining the data needed, and completing and reviewing this collection of information. Send comments regarding this burden estimate or any other aspect of this collection of information, including suggestions for reducing this burden to Washington Headquarters Services, Directorate for Information Operations and Reports, 1215 Jefferson Davis Highway, Suite 1204, Arlington, VA 22202-4302, and to the Office of Management and Budget, Paperwork Reduction Project (0704-0188), Washington, DC 20503

1. AGENCY USE ONLY (Leave blank)		2. REPORT DATE September 2002	3. REPORT TYPE AND DATES COVERED Annual (1 Sep 01 - 31 Aug 02)	
4. TITLE AND SUBTITLE Non-Invasive Monitoring of Breast Tumor Oxygenation: A Key to Tumor Therapy Planning and Tumor Prognosis			5. FUNDING NUMBERS DAMD17-00-1-0459	
6. AUTHOR(S) Hanli Liu, Ph.D.				
7. PERFORMING ORGANIZATION NAME(S) AND ADDRESS(ES) The University of Texas at Arlington Arlington, Texas 76019-0145 E-Mail: hanli@uta.edu			8. PERFORMING ORGANIZATION REPORT NUMBER	
9. SPONSORING / MONITORING AGENCY NAME(S) AND ADDRESS(ES) U.S. Army Medical Research and Materiel Command Fort Detrick, Maryland 21702-5012			10. SPONSORING / MONITORING AGENCY REPORT NUMBER	
11. SUPPLEMENTARY NOTES Original contains color plates: All DTIC reproductions will be in black and white.				
12a. DISTRIBUTION / AVAILABILITY STATEMENT Approved for Public Release; Distribution Unlimited			12b. DISTRIBUTION CODE 20030502 108	
13. ABSTRACT (Maximum 200 Words) The goal for Year 2 study includes 1) to modify the single-channel system into a 3-channel NIR system so that three measurements in both transmittance and reflectance geometry can be taken simultaneously, and 2) to investigate heterogeneity of HbO ₂ in the tumor vasculature of the rat breast tumors using the 3-channel NIR system. With a multi-channel NIRS system and the newly developed tumor hemodynamic phantoms, we have experimentally demonstrated that the previously observed, bi-phasic temporal changes in HbO ₂ of breast tumors under carbogen intervention can be associated with two perfusion rates or two blood flow rates. The newly developed hemodynamic phantoms are helpful to simulate the hemodynamic processes undertaken within the tumor tissues, and the phantoms will be further used in Year 3 study. Furthermore, we have further implemented and utilized FEMLAB computer software to mimic dynamic light distribution in a simulated tissue vasculature so as to understand the effects of tumor heterogeneity on the multi-channel NIR measurements. We plan to use FEMLAB for further experimental validations in animal measurements. Finally, after the implementation of the tunable 2-cm cooper coil and a plastic NIR source-detector coupler, we are ready to conduct the simultaneous measurements between FREEDOM and NIRS for the rat breast tumor measurements.				
14. SUBJECT TERMS: technology development, radiological sciences, tumor therapy planning and prognosis, tumor physiology monitoring			15. NUMBER OF PAGES 26	
			16. PRICE CODE	
17. SECURITY CLASSIFICATION OF REPORT Unclassified	18. SECURITY CLASSIFICATION OF THIS PAGE Unclassified	19. SECURITY CLASSIFICATION OF ABSTRACT Unclassified	20. LIMITATION OF ABSTRACT Unlimited	

NSN 7540-01-280-5500

Standard Form 298 (Rev. 2-89)
Prescribed by ANSI Std. Z39-18
298-102

Table of Contents

Cover.....	1
SF 298.....	2
Table of Contents.....	3
Introduction.....	4
Body.....	4
Key Research Accomplishments.....	15
Reportable Outcomes.....	15
Conclusions.....	16
References.....	16
Appendices.....	17

2001-2002 ANNUAL PROGRESS REPORT (YEAR 2)

This report presents the specific aims and accomplishments of our breast cancer research project during the second year of funding sponsored by the U.S. Department of the Army. It covers our activities from September 1, 2001 to October 31, 2002.

Introduction

The overall goal of this research project is to develop and evaluate a new approach to monitoring of oxygenated hemoglobin concentration (HbO_2) of breast tumors under respiratory interventions using near infrared (NIR) spectroscopy and imaging techniques. Furthermore, we wish to compare and validate the optical method with concurrent measurements of tumor oxygen tension with the use of ^{19}F EPI relaxation of hexafluorobenzene (HFB). Once we have rigorously established the integrated approach to tumor physiology, we will explore the influence of three interventions expected to modify tumor physiology. A better understanding of the interplay of these parameters in the natural history of a tumor could lead to enhanced therapeutic approaches and provide a novel diagnostic/prognostic tool for breast cancer research and clinical practice.

The overall project has four specific aims:

Aim 1: To evaluate a single-channel, dual wavelength, NIR, frequency-domain oximeter and the algorithms for obtaining tumor HbO_2 against tumor pO_2 measured by ^{19}F EPI relaxation of HFB.

Aim 2: To modify the single-channel system into a 3-channel NIR system.

Aim 3: To investigate heterogeneity of HbO_2 in breast tumors using the 3-channel NIR system.

Aim 4: To study the influence of three interventions on HbO_2 and pO_2 of the tumor simultaneously.

Specifically, Task 2 was planned for months 12-18 to accomplish Aim 2, and Task 3 was planned for months 18-24 to accomplish Aim 3:

Task 2: To modify the single-channel system into a 3-channel NIR system so that three measurements in both transmittance and reflectance geometry can be taken simultaneously, (*months 12-18*);

Task 3: To investigate heterogeneity of HbO_2 in the tumor vasculature of the rat breast tumors using the 3-channel NIR system (*months 18-24*).

Body of the Report

The PI and her graduate students have made significant efforts to accomplish the tasks. We have obtained an 8-channel NIR DC (i.e., not amplitude-modulated) system, which allows multi-channel simultaneous measurements in different locations. We have designed and developed a breast tumor dynamic phantom in order to perform 3-channel experiments with the multi-channel NIR system. We have conducted computer simulations to further support our hemodynamic phantom measurement and to understand the effects of tumor heterogeneity on the multi-channel NIR readings. Furthermore, we have implemented coupling components in preparation for the simultaneous measurements of NIR and ^{19}F EPI relaxation of HFB.

1. Tumor Hemodynamic Phantoms

1.1 Motivation and the Phantom Development

Our previous *in vivo* animal study has clearly demonstrated that cabogen (95% O₂ + 5% CO₂) inhalation can improve the vascular oxygen level of breast tumors monitored by NIR spectroscopy (NIRS)¹. The observed changes in tumor vascular oxygenation exhibited a rapid increase, followed by a gradual but significant increase, in response to carbogren intervention. We have earlier developed¹ a mathematical model to interpret this bi-phasic tumor hemodynamic feature: namely, tumor vasculature is comprised with a well-perfused and poorly perfused region. To provide actual support for this model and to further study heterogeneity of the breast tumor vasculature, we designed and developed a breast tumor dynamic phantom in order to perform 3-channel experiments with the multi-channel NIRS system.

Gel phantom was fabricated by adding 50 g of gelatin powder (Sigma, Gelatin Type A, St. Louis, MO) into a boiling intralipid solution, which consisted of 350 ml of water and 200 ml of intralipid (Intralipid® 20%, Baxter Healthcare Corp., Deerfield, IL 20%). The use of intralipid is to simulate light scattering in tumor tissues. The solution was stirred thoroughly until the gelatin powder was dissolved in the intralipid solution completely, and then the solution was cooled down at room temperature. Just before the solution started to be solidified, it was poured into a cylindrical container (diameter = 4.5 cm and height = 3.5 cm), which contained two small tubing networks used to simulate vascular networks. After completely being cooled down, the solution became a soft gelatin phantom with the two networks imbedded inside.

The two imbedded tube networks were used to simulate two distinct perfusion regions in a breast tumor. We wound a small-diameter (I.D.=0.52 mm) tube and an intermediate-diameter tube (I.D.=0.86 mm) to simulate well-perfused and poorly perfused region, respectively, on a big diameter core tube (O.D.=14 mm). An example of such a tubing network is shown in Figure 1. A stream of ink solution was used to go through the network to simulate a blood flow through the tumor vasculature. In this way, we could mimic a hemodynamic process of a breast tumor by changing the size or length of the small tube or by controlling the flow rate of the ink solution.

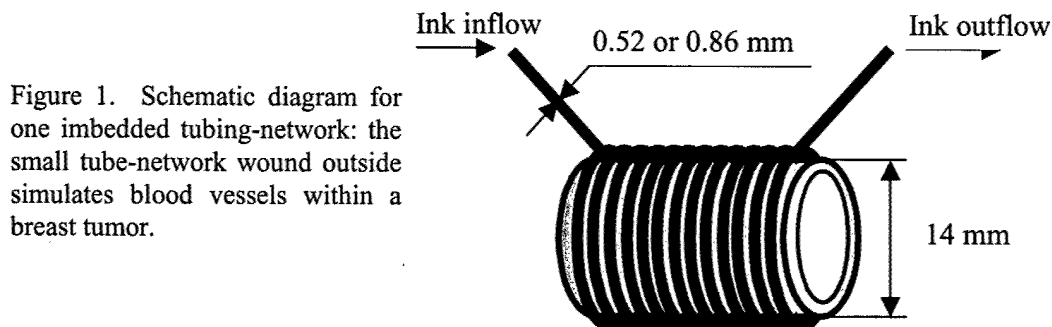


Figure 1. Schematic diagram for one imbedded tubing-network: the small tube-network wound outside simulates blood vessels within a breast tumor.

1.2 Experimental Setup for the Phantom Study

Experimental setup for the tumor phantom study with the multi-channel NIR system is shown in Figure 2. As shown here, three NIR optical detectors were placed on the side of the cylindrical phantom: two were placed in reflectance geometry with respect to the light source, whereas the other was in the transmission mode. With such a setup, the two detectors in the reflectance mode (D2 and D4) would get the NIR signals from only one of the individual tubing-networks, and the third detector (D1) in the transmission mode would detect the signal passing through both the networks.

During the measurement, the network tubes were filled with water, and a diluted black ink solution was used to simulate the light absorption effect of blood and was injected into only one tube, followed by a washout with water. Then, the experiment was conducted by injecting the ink solution into the second tube, and also followed by a washout of water. Finally, the ink solution was injected into both of the two tubes at the same time with the following washout water. Various flow rates (from 2 ml/hr to 40 ml/hr) were used to simulate different perfusion rates in tumors. Changes of light intensities were recorded with the computer through the entire experiment, and the time constants for the dynamic changes in light absorption were calculated by fitting the data using Kaleidagraph software (Synergy Software, Reading, PA).

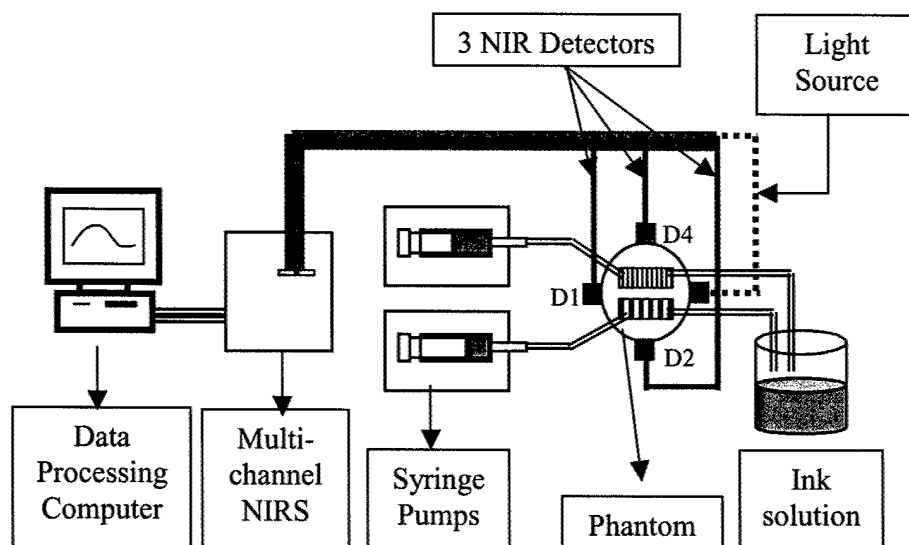


Figure 2. Experimental setup for the dynamic phantom study

As shown in Figure 2, detector 2 (D2) was placed on the side near the large diameter tube, and detector 4 (D4) was put near the small diameter tube. Detector 1 (D1) was placed just across the source about at the center between the two hidden networks. Therefore, we expected that D2 and D4 would get signals from only large diameter tube and small diameter tube, respectively, and D1 would obtain signals from both of the networks since it had similar distances to both of them.

1.3 Experimental Results of the Phantom Measurements

Figure 3 shows the absorption changes ($\Delta\mu_a$, wavelength=730 nm) of tumor phantom at three different positions when the ink solution was injected into the network tubes. The first step for this experiment was to inject the ink solution into only the large diameter tube with a flow rate of 20 ml/hr. As we can see from figure 3, the reading from D2 (pink trace) showed a largest increase in change of absorption, and D4 (green trace) showed the smallest increase in $\Delta\mu_a$. The $\Delta\mu_a$ increase measured from D1 (blue trace) was between those obtained from D2 and D4. A similar pattern is also shown at step 2, where the ink solution was injected only into the small diameter tube with the same flow rate (20 ml/hr). In this case, Figure 3 demonstrates that the signal from D4 had a largest increase in $\Delta\mu_a$, and D2 detected the smallest $\Delta\mu_a$ increase. This clearly demonstrates that signal from heterogeneity can be detected stronger if it is near the detector.

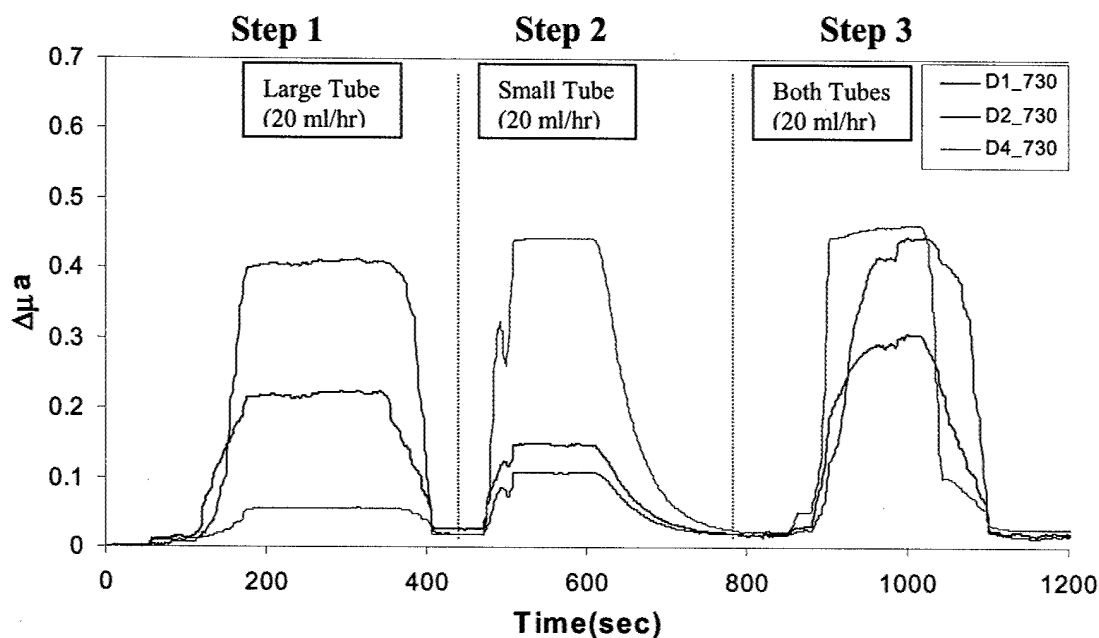


Figure 3. 3-channel NIRS results measured on a tumor dynamic phantom with two-size tubing networks. Three traces represent the readings at D1 (in transmission mode and located between the two tube networks), D2 (near the large tube), and D4 (near the small tube).

The third step in the measurement was to inject the ink solution into both of the tubes simultaneously with the same flow rate as before (20 ml/hr). At this step, we can observe two features: 1) the time profile taken at D4 (green trace) has a faster transition time than that at D2 (pink trace), and 2) the time profile taken at D1 (blue trace) has a bi-exponential characteristic, which is very similar to those we often observed in our breast tumor dynamic measurements¹.

To understand these phantom measurements, let us consider the velocities at each tube. Even though the flow rate was the same for both of the tubes, the velocities of the ink solutions in the two tube networks were different due to the different diameters. The solution in the small diameter tube had a velocity 2.74 times faster than that of the large diameter tube, based on the following relationship:

$$\frac{V_{small}}{V_{large}} = \frac{r_{large}^2}{r_{small}^2} = \frac{0.43^2}{0.26^2} = 2.74$$

where V_{small} and V_{large} are velocities of the ink solution in the small and large tubes, respectively, and r_{small} and r_{large} represent the radii of the small and large tubes, respectively. This velocity difference may be the reason why the transition time is faster in the small tube than that in the large tube. Furthermore, since D1 was in the transmission geometry and was located near both of the tube networks, the signal obtained at D1 should reflect the dynamic changes occurred in both of the tubes. We expect that the bi-exponential feature recorded by D1 results from a superposition between the two different dynamic transitions at the two networks.

The phantom data presented here basically demonstrate that we can experimentally mimic the bi-exponential behavior with two different velocities, or perfusion rates, from two different diameter networks. This knowledge may help us understand the bi-phasic features observed in the breast tumor vascular oxygenation measurements under carbogen inhalation. Furthermore, the next example demonstrates that the bi-exponential dynamics may also result from different flow rates, given the same diameters for the two tube networks.

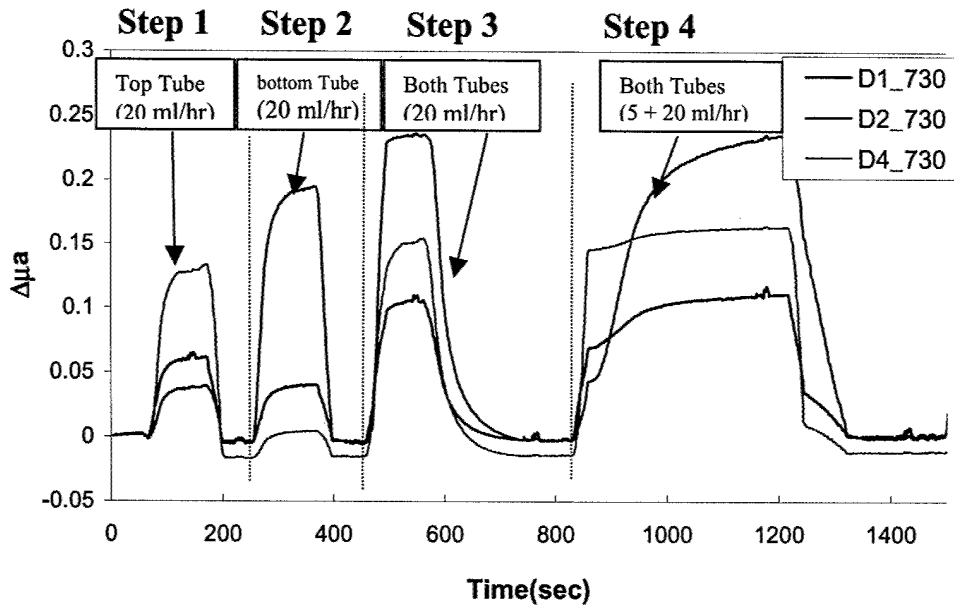


Figure 4. 3-channel NIRS results measured on a tumor dynamic phantom with two-size tubing networks. Three traces represent the readings at D1 (in transmission mode and located between the two tube networks), D2 (near the large tube), and D4 (near the small tube).

Figure 4 shows the experimental results from another phantom, where the two tubes have the same diameter and length, but with different controlled flow rates. By alternating the flow rate, we observed the results similar to those shown in Figure 3. The first step for this experiment was to inject the ink solution only into the top tube (near D4, Fig.2) with a flow rate of 20 ml/hr. As a result, D4 (green trace) showed the largest increase of $\Delta\mu_a$, while D2 (pink trace) showed the smallest increase of $\Delta\mu_a$ since D2 is quite away from the top network. For the second step, the bottom network (near D2) was injected with the ink solution at the same flow rate of 20 ml/hr. Here, D2 detected the largest increase of $\Delta\mu_a$, and D4 showed the smallest increase of $\Delta\mu_a$. In both of the above cases, the signals from D1 (blue trace) showed similar profiles as the others, without clear bi-exponential patterns. Then, as the third step, the ink solution was injected into both of the tube networks with the same flow rate (20 ml/hr). Similarly, we do not observe any clear features of the two-exponential increase of $\Delta\mu_a$. For the fourth step, we injected the solution into the tubes with two different flow rates: 20 ml/hr for the top tube and 5 ml/hr for the bottom tube. Now the data clearly show a bi-exponential behavior detected by D1.

Further time constant analysis helps understand the meaning of the two-exponential feature measured at D1. Fig. 5a shows a one-exponential fitting of the fast increase of $\Delta\mu_a$ obtained at D4, with a time constant, τ , of 20.9 ± 0.5 sec. Fig. 5b is a similar fitting for the signal at D2, with $\tau=121 \pm 3$ sec. Finally, Fig. 5c shows a two-exponential fitting for the signal at D1 with $\tau_1=18.1 \pm 0.9$ sec and $\tau_2=134 \pm 11$ sec for both the fast and slow components, respectively. The data clearly demonstrate that the time constant for the fast component, τ_1 , from D1 (18.1 sec) matches well with τ from D4 (20.9 sec), and τ_2 from D1 (134 sec) matches well with τ from D2 (121 sec). This suggests that the dynamic signals obtained from D1 with a fast and slow component indeed result from the dynamic changes in both of the tubes.

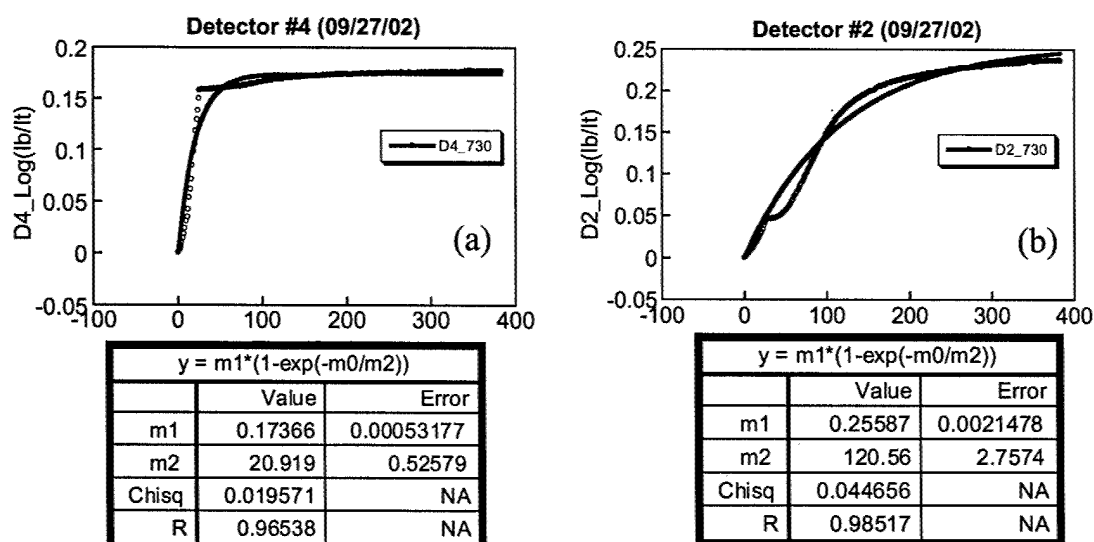


Figure 5 Temporal profiles of the NIRS measurements from D4 (a) and D2 (b) with the one-exponential fitting parameters shown at the bottom of each figure.

$y = m1*(1-\exp(-m0/m2))+m3*(1-\exp(-m0/m4))$		
	Value	Error
m1	0.068109	0.0024093
m2	18.129	0.87637
m3	0.046865	0.0017792
m4	133.65	11.354
Chisq	0.0018442	NA
R	0.99287	NA

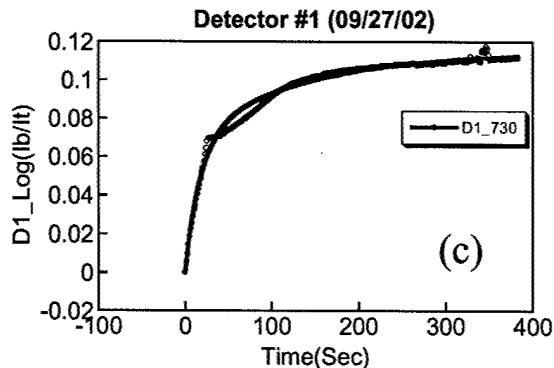


Figure 5c Temporal profile of the NIRS measurement from D1 with the bi-exponential fitting parameters shown on the left.

As shown above, these dynamic fast- and slow-changes simulate very well the changes observed in our breast tumor oxygenation measurements, supporting our hypothesis¹ that the bi-phasic tumor hemodynamic feature results from a well-perfused and poorly perfused region in the tumor vasculature under carbogen interventions. In this way, the multi-channel NIRS system allows us to study the dynamic heterogeneity at different locations, showing that the tumor vasculature in the poorly perfused region (with a lower perfusion rate) can be eventually oxygenated if the two dynamic components are observed. On the other hand, if only the fast component exists, it suggests that the poorly perfused region in the tumor may not have much chance to be improved for its vascular oxygenation under carbogen intervention.

2. Computer Simulations to Understand the Phantom Experiments

To further support our tumor hemodynamic phantom study, we used FEMLAB software to simulate the dynamic process of light distribution as well as the NIR measurement in tissues, such as in breast tumors. In this way, we can better understand the effects of tumor heterogeneity on the multi-channel NIR measurements.

2.1 Introduction to FEMLAB

Based on the Finite Element Method (FEM), FEMLAB is interactive computer software and developed by the COMSOL Group (COMSOL Inc. Burlington, MA). It uses numerical approaches to solve Partial Differential Equations (PDE) in modeling and simulating various engineering problems. The FEMLAB Graphical User Interface (GUI) is used for the modeling process by using ready-to-use application modules or by using equation-based modeling. In general, several of ready-to-use application modules are commercially available for engineering problems: such as chemical engineering modules, electromagnetic module, and structural mechanics module. FEMLAB solves different systems of equations simultaneously by using multi-physics modeling, and FEMLAB models can also be used with various MATLAB toolboxes.

2.2 Simulation of Light Propagation in Tumor Tissue

According to diffusion theory, the simulation problem starts with a PDE to describe the light propagation in the tumor tissue as follows:

$$\nabla^2 \psi(r) - \frac{\mu_a}{D} \psi(r) = S_0(r)$$

where $\psi(r)$ is the light distribution at position r inside the tumor tissue, $\mu_a = 0.1 \text{ cm}^{-1}$ is the absorption coefficient, $D = 0.033 \text{ cm}$ is the diffusion coefficient, and $S_0(r)$ is the light source term. The boundary condition for light propagation in the simulated tumor tissue is given by

$$\psi(r) - 2AD\hat{n} \cdot \nabla \psi(r) = 0.$$

In the simulation, the Neumann Boundary condition was used with the various parameters specified as: Internal reflection $A = 2.9193$ and $D = 0.033 \text{ cm}$. The simulation model was then meshed in the mesh mode using 1147 elements and 609 nodes. Finally, it is solved using the stationary nonlinear solver type.

Specifically, the geometry for the FEM tumor simulations is shown in Figure 6, and it mimics a 2-dimensional horizontal cross section of our tumor phantom. E1 represents the body of tumor phantom (diameter = 4 cm), and R5 shows location of the light source. Furthermore, each tube used in the dynamic phantom is represented by two rectangles (0.1 x 2.4 cm rectangle) as a blood vessel network: R1 and R2 are representing vessels with a fast flow rate, and R3 and R4 denote vessels with a slow flow rate.

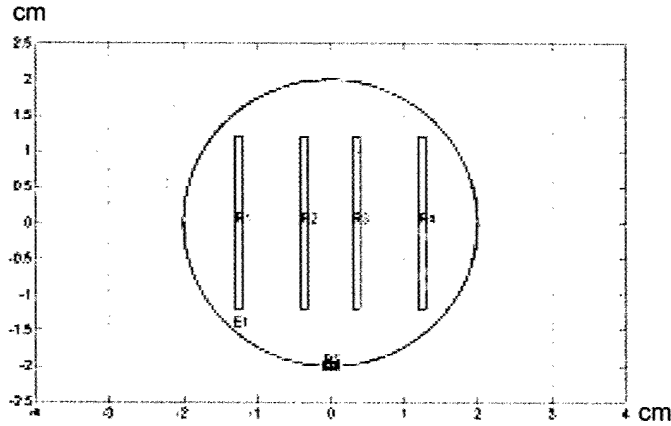


Figure 6 Geometry for FEM simulations of a breast tumor.

The diffusion equation has been selected to predict photon distribution in the phantom as the ink solution flows through the tubes. Absorption coefficients for the background phantom and tubes were 0.03 and 1.5 cm^{-1} , respectively. We also used 0.03 cm as the diffusion coefficient of the phantom since it gives a reduced scattering coefficient of 10 cm^{-1} .

2.3 Simulation Results of the Tumor Dynamics

Different flow rates used in the phantom study were simulated by changing the tube size with different frame rates. In other words, a fast flow rate was simulated by increasing the tube length with a large increment per frame (e.g., 0 to 2.4 cm with 0.6 cm increment per frame), and a slow flow rate was simulated by increasing tube length with a small increment (0 to 2.4 cm with 0.02 cm increment per frame). In this way, a flow rate difference between the two tubes can be established.

Figure 7 shows an example of the FEM tumor phantom simulation. Figure 7a is the light distribution of a dynamic phantom, where there was ink injection into only the left tube with a fast flow rate. Figure 7b is the simulation when the ink solution flowed into only the right tube with a slow flow rate. With the same frame rate, Figure 7a is the result of the simulation at the 6th frame, while Figure 7b is simulated for the 120th frame. This implies that the left tube has a flow rate 20 times faster than the right tube.

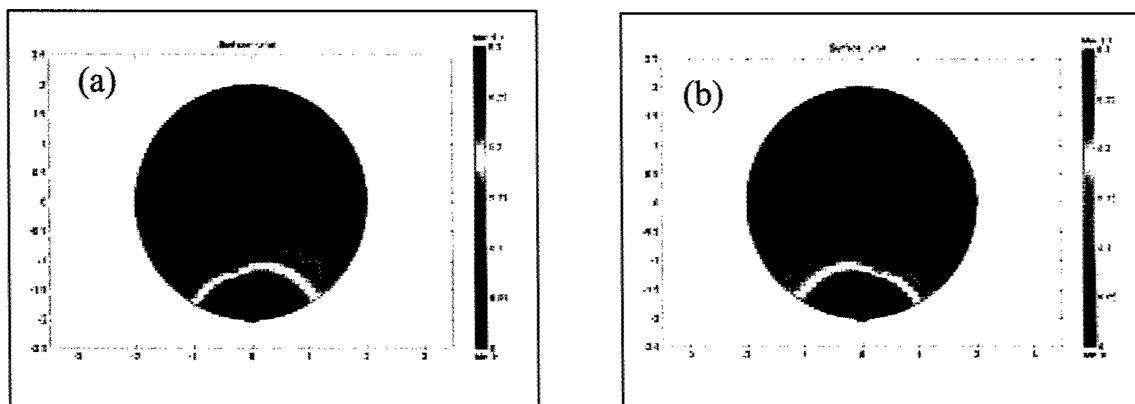


Figure 7 FEM simulations of light distribution inside of a dynamic phantom.(a): the results with a fast simulated flow rate; (b): the results with a slow flow rate at a later time.

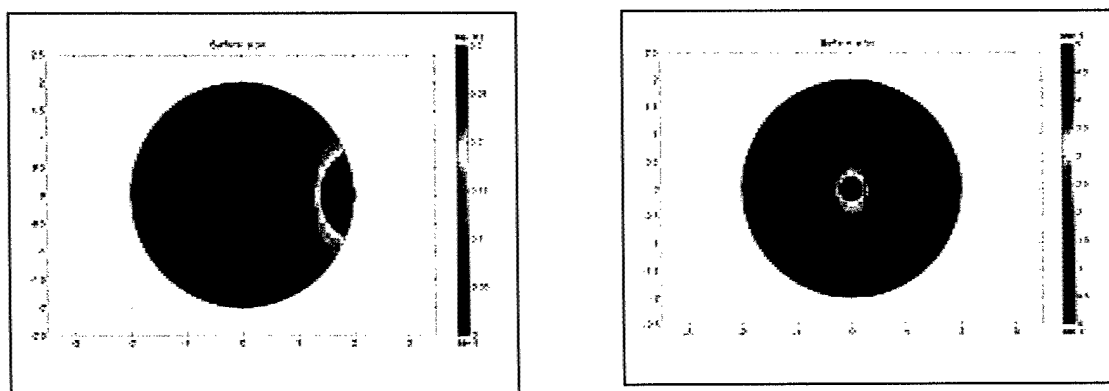


Figure 8 FEM simulations of light distribution inside of a dynamic phantom. (a): the results with a fast simulated flow rate; (b): the results with a slow flow rate.

We also changed the position of the light source to see the effect of vessel/tube geometry on bi-phasic feature of the tumor hemodynamic measurements. We changed the position of the light source to the right side of the phantom (Fig. 8a) and to the center of the phantom (Fig. 8b). In the geometry of Fig. 8a, the light penetrates the slow-flow object first and then the fast-flow object. This simulation was done to find whether in this geometry, the light signal changes still have the two-exponential behavior. In other words, we wish to investigate whether the bi-phasic hemodynamic feature depends on the orientations of the vessels/tube networks. We are in the continuation for this study. Furthermore, we are also in the process of comparing the simulation results with those obtained in the phantom experiments, particularly to compare the time constants.

3. Simultaneous Measurement using NIR and ^{19}F EPI relaxation of HFB

To prepare ourselves for Aim 4, which is to study the influence of three interventions on HbO_2 and pO_2 of the tumor simultaneously, we have conducted the following work for simultaneous measurements using multi-channel NIRS and ^{19}F EPI relaxation of HFB (Hexafluorobenzene).

3.1 Animal & tumor model:

NF13762 mammary adenocarcinomas were implanted in skin pedicles on the forebacks of the female Fisher 344 rats (~150g) until tumors reach approximately 1 cm in diameter. The measurements would be taken when the tumor had a diameter of 1 cm, 1.5 cm, and 2 cm. Rats were anesthetized with 150 μL Ketamine hydrochloride (100 mg/ml, i.p.) and maintained under general gaseous anesthesia with 1.3% isoflurane in air (1 dm^3/min).

20 μL of Hexafluorobenzene (PCR Inc., Fainesville, FL) was injected directly into the tumor, either centrally or peripherally in a single plane using a Hamilton syringe (Reno, NV) with a sharp needle (32 gauge). The needle was inserted manually to penetrate across the whole tumor and withdrawn ~1 mm to reduce the tissue pressure, and 2~5 μL of HFB were injected. The needle was repeatedly withdrawn at a step size of 1~2 mm and further HFB injected. A total of 2~3 tracks of HFB were injected in the form of a fan shape.

The rat was placed on its side in a cradle with a thermal blanket to maintain body temperature at 37°C. A home-built tunable and matchable 2 cm cooper coil was made and placed around the tumor with the tumor centered inside the coil. In addition, a sealed capillary tube of HFB doped with benzene (as a shift agent) was placed alongside the tumor. This provided a quantitative standard with approximately 3 ppm offset from the intra-tumoral HFB, allowing clearance from the tumor to be assessed. A home-built plastic NIR source-detector fixer was also made to fix the two NIR fiber bundle tips around the receiver coil within the MRI facility, as shown in Figure 9.

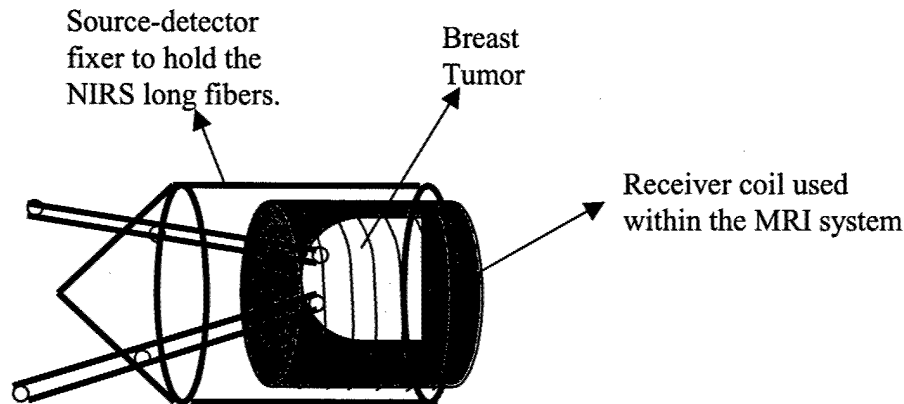


Fig 9. Home-built plastic NIR source-detector fixer with a receiver coil.

3.2 MRI scanner and RF coils

All in vivo MRI experiments were performed on an Omega CSI 4.7 T superconducting magnet with actively shielded gradients. The magnet operated at a proton (^1H) frequency of 200.106 MHz and a fluorine (^{19}F) frequency of 188.273 MHz. It consisted of the Omega software that can accomplish data acquisition and analysis with the UNIX operating system. Two single-turn solenoid coils (1.5 cm and 2.5 cm) were built for this study. Their sizes matched the tumor sizes.

3.3 NIR spectroscopy

NIR spectroscopy uses commercially available in-phase and quadrature (IQ) demodulator chips to demodulate the detected, amplitude-modulated optical signals. 22-foot long fibers with a diamagnetic material for the probe tips were used within the magnetic field to transmit the laser light to the tumor and to detect the optical signal from the tumor. The reason to use 22-foot long fibers is to keep the NIR oximeter away from the magnetic field. Three of home-built converters have been made for the long fiber bundles to couple with the home-built connector.

3.4 Investigation of Tumor pO_2 with FREDOM and HbO_2 with NIR

Currently for this study, we are in the process of using the FREDOM approach (Fluorocarbon Relaxometry using Echo planar imaging for Dynamic Oxygen Mapping) based on hexafluorobenzene (HFB) to measure tumor pO_2 and the NIRS system to measure HbO_2 simultaneously.

The respiratory challenge paradigm for the rats will be:

air \rightarrow 100% $\text{O}_2 \rightarrow$ air \rightarrow 95% O_2 + 5% CO_2 (carbogen) \rightarrow air

Key Research Accomplishments

- 1) We have obtained and tested a multi-channel NIRS system for simultaneous dynamic oxygenation measurements at different locations of breast tumors.
- 2) We have developed breast tumor hemodynamic phantoms and conducted multi-channel NIRS measurements on the newly developed phantoms to simulate the dynamic HbO₂ changes of rat breast tumors under hyperoxic inhalations. This study supports our earlier dynamic model to explain the bi-phasic dynamic oxygenation process of breast tumors under hyperoxic interventions.
- 3) We have further implemented and utilized FEMLAB computer software to mimic dynamic light distribution in a simulated tissue vasculature so as to understand the effects of tumor heterogeneity on the multi-channel NIR measurements.
- 4) We have implemented home-built tunable 2 cm cooper coil, which will be placed around the rat breast tumor within the MRI facility during the simultaneous measurements between FREDOM and NIRS. Also, a home-built plastic NIR source-detector coupler (fixer) was made to hold the two NIR fiber bundle tips around the receiver coil within the MRI. This work is done to prepare for experiments needed for Aim 4.

Reportable Outcomes

Peer-reviewed Journals:

1. Jae G. Kim, Yulin Song, Dawen Zhao, Anca Constantinescu, Ralph P. Mason, and **Hanli Liu**, "Interplay of Tumor Vascular Oxygenation and Tumor pO₂ Observed Using NIRS, Oxygen Needle Electrode, and ¹⁹F MR pO₂ Mapping," *J. of Biomedical Optics* in press (2002).
2. Yueqing Gu, Vincent Bourke, Jae G. Kim, Anca Constantinescu, Ralph P. Mason, **Hanli Liu** "Dynamic Response of Breast Tumor Oxygenation to Hyperoxic Respiratory Challenge Monitored with Three Oxygen-Sensitive Parameters," submitted to *Applied Optics*, 2002.
3. Mengna Xia and **Hanli Liu**, "Determination of Total Hemoglobin Concentrations in Blood-Perfused Turbid Media with Scattering Variations," in preparation.
4. Yueqing Gu, **Hanli Liu**, Yulin Song, Anca Constantinescu, Ralph P. Mason, "Vascular oxygenation dynamics of breast tumors in response to therapeutic interventions monitored by Near Infrared Spectroscopy," in preparation.
5. Jae Kim, Ralph P. Mason, and **Hanli Liu**, "Investigation of Tumor Hemodynamics: Dynamic Phantoms and FEM Simulations," in preparation.

Presentations and Proceeding Papers:

1. Jae G. Kim, Yuling Song, **Hanli Liu**, Anca Constantinescu, and Ralph P. Mason, "Investigation of tumor oxygen consumption and tumor vascular oxygen dynamics in response to pharmacological interventions by NIRS," *OSA Biomedical Topical Meetings*, Technical Digest, SuH2, Miami Beach, FL, April 7-10, 2002.
2. Yulin Song, Yueqing Gu, Jae G. Kim, **Hanli Liu**, Anca Constantinescu, and Ralph P. Mason, "Correlation between total hemoglobin concentration and blood volume of breast tumors measured by NIR spectroscopy and ^{19}F MRS of PFOB," *OSA Biomedical Topical Meetings*, Technical Digest, SuH5, Miami Beach, FL, April 7-10, 2002.
3. **Hanli Liu**, "Near-Infrared Spectroscopy Used in vivo for Assisting Neurosurgery and Tumor Oximetry," Workshop on Biotechnology and Nano-biotechnology—Challenges and Opportunities of Drug Targeting in the Post Genomic Era, organized by the University of Texas at Dallas and the University of Texas Southwestern Medical Center at Dallas, Dallas, October 18, 2001.
4. J. G. Kim, Y. Song, D. Zhao, A. Constantinescu, R. P. Mason, and **Hanli Liu**, "Interplay of Tumor Vascular Oxygenation and pO_2 in Tumors Using NIRS and Needle Electrode," *Proc. SPIE-Int. Soc. Opt. Eng.* 4250, 429-436 (2001).

Conclusions

From the work that we have conducted in Year 2, we can draw the following conclusions:

- 1) With a multi-channel NIRS system and the newly developed tumor hemodynamic phantoms, we have experimentally demonstrated that the previously observed, bi-phasic temporal changes in HbO_2 of breast tumors under carbogen intervention can be associated with two perfusion rates or two blood flow rates.
- 2) The newly developed hemodynamic phantoms are helpful to simulate the hemodynamic processes undertaken within the tumor tissues, and the phantoms will be further used in Year 3 study.
- 3) FEMLAB has proven to be valuable in simulating the light propagation in the breast tumor tissue and the corresponding NIRS measurements, and we plan to use FEMLAB for further experimental validations in both laboratory and animal measurements.
- 4) After the implementation of the home-built, tunable 2-cm cooper coil and a home-built plastic NIR source-detector coupler, it is feasible and ready to conduct the simultaneous measurements between FREDOM and NIRS.

References:

-
- ¹ H. Liu, Y. Song, K. L. Worden, X. Jiang, A. Constantinescu and R. P. Mason, "Noninvasive investigation of blood oxygenation dynamics of tumors by near-infrared spectroscopy," *Appl. Opt.*, **39**, pp. 5231-5243 (2000).

Interplay of tumor vascular oxygenation and tumor pO_2 observed using near-infrared spectroscopy, an oxygen needle electrode, and ^{19}F MR pO_2 mapping

Jae G. Kim

University of Texas at Arlington/University of Texas
Southwestern Medical Center at Dallas
Joint Graduate Program in Biomedical Engineering
Arlington, Texas 76019

Dawen Zhao

University of Texas Southwestern Medical
Center at Dallas
Advanced Radiological Sciences
Department of Radiology
Dallas, Texas 75390

Yulin Song

University of Texas at Arlington/University of Texas
Southwestern Medical Center at Dallas
Joint Graduate Program in Biomedical Engineering
Arlington, Texas 76019
and
University of Texas Southwestern Medical
Center at Dallas
Advanced Radiological Sciences
Department of Radiology
Dallas, Texas 75390

Anca Constantinescu

Ralph P. Mason

University of Texas Southwestern Medical
Center at Dallas
Advanced Radiological Sciences
Department of Radiology
Dallas, Texas 75390

Hanli Liu

University of Texas at Arlington/University of Texas
Southwestern Medical Center at Dallas
Joint Graduate Program in Biomedical Engineering
Arlington, Texas 76019

Abstract. This study investigates the correlation of tumor blood oxygenation and tumor pO_2 with respect to carbogen inhalation. After having refined and validated the algorithms for calculating hemoglobin concentrations, we used near-infrared spectroscopy (NIRS) to measure changes of oxygenated hemoglobin concentration ($\Delta[HbO_2]$) and used an oxygen needle electrode and ^{19}F MRI for pO_2 measurements in tumors. The measurements were taken from Dunning prostate R3327 tumors implanted in rats, while the anesthetized rats breathed air or carbogen. The NIRS results from tumor measurements showed significant changes in tumor vascular oxygenation in response to carbogen inhalation, while the pO_2 electrode results showed an apparent heterogeneity for tumor pO_2 response to carbogen inhalation, which was also confirmed by ^{19}F MR pO_2 mapping. Furthermore, we developed algorithms to estimate hemoglobin oxygen saturation, sO_2 , during gas intervention based on the measured values of $\Delta[HbO_2]$ and pO_2 . The algorithms have been validated through a tissue-simulating phantom and used to estimate the values of sO_2 in the animal tumor measurement based on the NIRS and global mean pO_2 values. This study demonstrates that the NIRS technology can provide an efficient, real-time, noninvasive approach to monitoring tumor physiology and is complementary to other techniques, while it also demonstrates the need for an NIR imaging technique to study spatial heterogeneity of tumor vasculature under therapeutic interventions. © 2003 Society of Photo-Optical Instrumentation Engineers. [DOI: 10.1117/1.1527049]

Keywords: frequency-domain spectroscopy; NIR spectroscopy; ^{19}F MRI; tumor vascular oxygenation; pO_2 electrode; oxygen; oximetry.

Paper 01078 received Nov. 13, 2001; revised manuscript received June 25, 2002; accepted for publication Aug. 26, 2002.

1 Introduction

It has long been known that hypoxic tumor cells are more resistant to radiation therapy than well-oxygenated tumor cells.¹ Breathing elevated oxygen (100%) or carbogen (95% O_2 , 5% CO_2) has been used during therapy for an attempt to improve tumor oxygenation.^{2,3} To monitor tumor tissue oxygen tension⁴ and its dynamic changes under respiratory interventions, various methods are available, including fiber optic sensors,⁵ oxygen electrodes,⁶ and electron spin resonance.⁷ MRI has the further advantage of providing dynamic maps of pO_2 , which can reveal tumor heterogeneity.⁸ While NIRS does not quantify pO_2 , it can indicate dynamic changes in vascular oxygenation and has the advantage of being entirely noninvasive, providing real-time measurements, and being cost-effective and portable. Furthermore, it would be important to correlate the changes between tissue pO_2 and vascular

oxygenation of the tumors since little is known about oxygen transfer from the tumor vasculature to tumor tissue.

The basic principle of NIRS rests on the fact that oxygenated and deoxygenated hemoglobin molecules are major chromophores in tissue in the near-infrared region (700 to 900 nm), and they exhibit distinct absorption characteristics. In principle, the concentrations of oxygenated hemoglobin [HbO_2], deoxygenated hemoglobin [Hb], and oxygen saturation of hemoglobin sO_2 can be determined by measuring light absorption and scattering in tissue based on diffusion theory. However, the theory works well only for large and homogeneous media.^{9,10} Accurate quantification of tumor oxygenation in our approach is currently limited to relative changes in [HbO_2] and [Hb] due to considerable heterogeneity and finite size of tumors.

The goal of this study was to investigate the correlation of tumor blood oxygenation and tumor pO_2 in response to car-

Address all correspondence to Hanli Liu. Tel: 817-272-2054; Fax: 817-272-2251; E-mail: hanli@uta.edu

bogen intervention and to develop a suitable algorithm to estimate the hemoglobin oxygen saturation of the tumor under the intervention. Specifically, in Sec. 2 of this paper, we derive accurate expressions for calculating changes in $[\text{HbO}_2]$ and $[\text{Hb}]$ to compensate for the differences in optical path length at two wavelengths and an algorithm to estimate absolute sO_2 values of the tumor during gas intervention. The algorithms are validated through tissue-simulating phantoms and used to estimate tumor sO_2 in the animal measurement using the NIRS and mean pO_2 values, as mentioned in Secs. 3 and 4. In Sec. 4, we will show that while NIRS results tended to be similar for several tumors, pO_2 electrode measurements showed considerable variation even in the same tumor type, suggesting distinct tumor heterogeneity. In Sec. 5, we discuss the need to develop an NIR imaging technique in order to study spatial heterogeneity of tumor vasculature under oxygen interventions. Finally, we conclude that the NIRS technology can provide an efficient, real-time, noninvasive approach to monitoring tumor physiology and is complementary to other techniques.

2 Theory and Algorithm Development

2.1 Algorithms to Quantify Changes in $[\text{HbO}_2]$ and $[\text{Hb}]$

NIR spectroscopy can be used to measure hemoglobin concentrations and oxygen saturation since light absorptions of HbO_2 and Hb are different at the wavelengths selected (758 and 785 nm). In common with our previous work,¹¹ we assumed that HbO_2 and Hb are the only significant absorbing materials in tumors within the selected NIR range of 700 to 900 nm. Based on Beer-Lambert's law, the absorption coefficients μ_a comprise the extinction coefficients for deoxyhemoglobin (ϵ_{Hb}) and oxyhemoglobin (ϵ_{HbO_2}) multiplied by their respective concentrations:

$$\mu_a^{758} = 2.3\{\epsilon_{\text{Hb}}^{758}[\text{Hb}] + \epsilon_{\text{HbO}_2}^{758}[\text{HbO}_2]\}, \quad (1)$$

$$\mu_a^{785} = 2.3\{\epsilon_{\text{Hb}}^{785}[\text{Hb}] + \epsilon_{\text{HbO}_2}^{785}[\text{HbO}_2]\}, \quad (2)$$

where the factor of 2.3 results from the different definitions of μ_a and ϵ in relation to the incident and detected optical intensities. The conventional definitions for μ_a and ϵ are $I = I_0 \exp(-\mu_a L)$ and $I = I_0 10^{-\epsilon CL}$, respectively, where I_0 and I are the incident and detected optical intensities in transmission measurement of a nonscattering medium, C is the concentration of hemoglobin measured in millimoles per liter, and L is the optical path length through the medium in centimeters. Therefore, we should have a relationship of $\mu_a = 2.3 \epsilon C$.

We have not yet completed a suitable algorithm to compute μ_a of rat tumors due to their finite size and high heterogeneity. Instead of diffusion theory, we modified Beer-Lambert's law, i.e., $\mu_a = 2.3 \epsilon C = (2.3/L) \log(I_0/I)$, to analyze the data using only amplitude values to quantify changes in $[\text{HbO}_2]$ and $[\text{Hb}]$. In this case, I_0 is the detected light intensity when no absorption is present. Specifically, changes in absorption coefficient of the tumor, $\Delta\mu_a$, between baseline and transient conditions under respiratory intervention can be expressed as

$$\Delta\mu_a = \mu_{aT} - \mu_{aB} = 2.3 \log(A_B/A_T)/L, \quad (3)$$

where L is the optical path length and A_B and A_T are baseline and transient amplitudes of the measured optical signals, respectively.

By manipulating Eqs. (1) to (3), changes of $[\text{HbO}_2]$ and $[\text{Hb}]$ due to an intervention can be expressed using the transmitted amplitudes of the light through the tumor as:

$$\Delta[\text{HbO}_2] = -11.73 \frac{\log(A_B/A_T)^{758}}{L^{758}} + 14.97 \frac{\log(A_B/A_T)^{785}}{L^{785}}, \quad (4)$$

$$\Delta[\text{Hb}] = 8.09 \frac{\log(A_B/A_T)^{758}}{L^{758}} - 6.73 \frac{\log(A_B/A_T)^{785}}{L^{785}}, \quad (5)$$

where L^{758} and L^{785} are optical path lengths between the source and detector at 758 and 785 nm, respectively. The units of $\Delta[\text{HbO}_2]$ and $\Delta[\text{Hb}]$ in Eqs. (4) and (5) are in millimolar. The constants given in the equations were computed with the extinction coefficients for oxygenated and deoxygenated hemoglobin at the two wavelengths used.¹² The constant values are slightly different from our previous report¹¹ due to a slight shift in wavelength (782 to 785 nm) from one laser source, but the actual differences between the values of $\Delta[\text{HbO}_2]$ and $\Delta[\text{Hb}]$ calculated from our previous report and from Eqs. (4) and (5) are little and negligible.

In principle, L^{758} and L^{785} given in Eqs. (4) and (5) are not constants, depending on both the source-detector separation and the optical properties of the measured medium. Optical path length in a scattering medium L has been expressed¹³ as the source-detector separation d multiplied by a differential pathlength factor (DPF), i.e., $L = d \times \text{DPF}$. DPF values of blood-perfused tissues should be wavelength- and oxygenation-dependent, and they have been studied intensively for muscles¹⁴ and brains¹⁵ with approximate values of 4 to 6 and 5 to 6, respectively. Little is known about DPF for tumors although a DPF value of 2.5 has been used by others.¹⁶ In our approach, we define two parameters, β_{HbO_2} and β_{Hb} , as ratios between DPF^{758} and DPF^{785} for oxygenated blood and deoxygenated blood, respectively, as given below:

$$\beta_{\text{HbO}_2} = \left(\frac{\text{DPF}^{758}}{\text{DPF}^{785}} \right)_{\text{HbO}_2} = \left(\frac{L^{758}}{L^{785}} \right)_{\text{HbO}_2},$$

$$\beta_{\text{Hb}} = \left(\frac{\text{DPF}^{758}}{\text{DPF}^{785}} \right)_{\text{Hb}} = \left(\frac{L^{758}}{L^{785}} \right)_{\text{Hb}}. \quad (6)$$

Substituting Eq. (6) into Eqs. (4) and (5) leads to

$$\Delta[\text{HbO}_2] = \frac{-\frac{11.73}{\beta_{\text{HbO}_2}} \log\left(\frac{A_B}{A_T}\right)^{758} + 14.97 \log\left(\frac{A_B}{A_T}\right)^{785}}{d \times \text{DPF}_0}, \quad (7)$$

$$\Delta[\text{Hb}] = \frac{\frac{8.09}{\beta_{\text{Hb}}} \log\left(\frac{A_B}{A_T}\right)^{758} - 6.73 \log\left(\frac{A_B}{A_T}\right)^{785}}{d \times \text{DPF}_0}, \quad (8)$$

where DPF_0 is a mean DPF at 785 nm for both oxygenated and deoxygenated states, i.e., $\text{DPF}_0 = \text{DPF}_{\text{HbO}_2}^{785} = \text{DPF}_{\text{Hb}}^{785}$, which is assumed to be the same for both $\Delta[\text{HbO}_2]$ and $\Delta[\text{Hb}]$. This assumption is based on the fact that the absorption difference between oxygenated and deoxygenated blood at 785 nm is much smaller than that at 758 nm. The maximal relative error caused by this assumption in tumor oxygen interventions was estimated to be less than 12%, and detailed justification and discussion were given in Ref. 11. Since our focus is on dynamic changes in tumor $[\text{HbO}_2]$ under carbogen intervention, we simplify Eqs. (7) and (8) to Eqs. (9) and (10) by including DPF_0 in the unit:

$$\Delta[\text{HbO}_2] = \frac{-\frac{11.73}{\beta_{\text{HbO}_2}} \log\left(\frac{A_B}{A_T}\right)^{758} + 14.97 \log\left(\frac{A_B}{A_T}\right)^{785}}{d}, \quad (9)$$

$$\Delta[\text{Hb}] = \frac{\frac{8.09}{\beta_{\text{Hb}}} \log\left(\frac{A_B}{A_T}\right)^{758} - 6.73 \log\left(\frac{A_B}{A_T}\right)^{785}}{d}, \quad (10)$$

where the units for Eqs. (9) and (10) become mM/DPF₀.

To further quantify β_{HbO_2} and β_{Hb} , we associate L to μ_a by $L = (\sqrt{3}/2)d (\mu_s'/\mu_a')^{1/2}$, where μ_s' is the reduced scattering coefficient, according to Sevick et al.¹⁰ and Liu.¹⁷ Equation (6) becomes

$$\beta_{\text{HbO}_2} = \left(\frac{L^{758}}{L^{785}}\right)_{\text{HbO}_2} = \left[\left(\frac{\mu_a^{758}}{\mu_a^{785}}\right)^{1/2}\right]_{\text{HbO}_2} = \left[\left(\frac{\epsilon^{758}}{\epsilon^{785}}\right)^{1/2}\right]_{\text{HbO}_2}, \quad (11)$$

$$\beta_{\text{Hb}} = \left(\frac{L^{758}}{L^{785}}\right)_{\text{Hb}} = \left[\left(\frac{\mu_a^{758}}{\mu_a^{785}}\right)^{1/2}\right]_{\text{Hb}} = \left[\left(\frac{\epsilon^{758}}{\epsilon^{785}}\right)^{1/2}\right]_{\text{Hb}}, \quad (12)$$

where $\mu_a = 2.3 \epsilon C$ and μ_s' values at two wavelengths are canceled, assuming that $\mu_s'(758 \text{ nm}) \cong \mu_s'(785 \text{ nm})$. By calculating the hemoglobin extinction coefficients at 758 and 785 nm,¹² we obtained $\beta_{\text{HbO}_2} = 1.103$ and $\beta_{\text{Hb}} = 0.9035$. Substituting these values into Eqs. (9) and (10) results in the final expressions for $\Delta[\text{HbO}_2]$ and $\Delta[\text{Hb}]$:

$$\Delta[\text{HbO}_2] = \frac{-10.63 \log\left(\frac{A_B}{A_T}\right)^{758} + 14.97 \log\left(\frac{A_B}{A_T}\right)^{785}}{d}, \quad (13)$$

$$\Delta[\text{Hb}] = \frac{8.95 \log\left(\frac{A_B}{A_T}\right)^{758} - 6.73 \log\left(\frac{A_B}{A_T}\right)^{785}}{d}. \quad (14)$$

$\Delta[\text{Hb}_{\text{total}}]$ can also be obtained by adding Eqs. (13) and (14):

$$\begin{aligned} \Delta[\text{Hb}_{\text{total}}] &= \Delta[\text{HbO}_2] + \Delta[\text{Hb}] \\ &= \frac{-1.68 \log\left(\frac{A_B}{A_T}\right)^{758} + 8.24 \log\left(\frac{A_B}{A_T}\right)^{785}}{d}. \end{aligned} \quad (15)$$

Equations (13) to (15) will be used in calculating $\Delta[\text{HbO}_2]$, $\Delta[\text{Hb}]$, and $\Delta[\text{Hb}_{\text{total}}]$ in tissue phantoms and tumors during gas interventions in this paper.

The units for $\Delta[\text{HbO}_2]$, $\Delta[\text{Hb}]$, and $\Delta[\text{Hb}_{\text{total}}]$ in Eqs. (13) to (15) are mM/DPF₀, which is still a variable, depending on the optical properties of the tumor at a particular wavelength. Since our study involves changes in $[\text{HbO}_2]$ due to respiratory challenges, we can obtain a normalized $\Delta[\text{HbO}_2]$ at its maximal value, i.e., $\Delta[\text{HbO}_2]/\Delta[\text{HbO}_2]_{\text{max}}$, to eliminate the unit so as to minimize the effect of DPF on our results. Next, we will show that a normalized $\Delta[\text{HbO}_2]$ has a close relationship with hemoglobin oxygen saturation $s\text{O}_2$.

2.2 Relationship Among Normalized $\Delta[\text{HbO}_2]$, $s\text{O}_2$ and Blood $p\text{O}_2$

We define $s\text{O}_2$ values of the measured sample at the baseline, transient state, and maximal state, i.e., $(s\text{O}_2)_{\text{base}}$, $(s\text{O}_2)_t$, and $(s\text{O}_2)_{\text{max}}$, respectively:

$$(s\text{O}_2)_{\text{base}} = \frac{[\text{HbO}_2]_{\text{base}}}{[\text{Hb}_{\text{total}}]_{\text{base}}}, \quad (16)$$

$$(s\text{O}_2)_t = \frac{[\text{HbO}_2]_t}{[\text{Hb}_{\text{total}}]_t}, \quad (17)$$

$$(s\text{O}_2)_{\text{max}} = \frac{[\text{HbO}_2]_{\text{max}}}{[\text{Hb}_{\text{total}}]_{\text{max}}}, \quad (18)$$

where $[\text{HbO}_2]_{\text{base}}$, $[\text{HbO}_2]_t$, and $[\text{HbO}_2]_{\text{max}}$ are corresponding to oxygenated hemoglobin concentrations at the respective state. Mathematically, it follows that

$$\begin{aligned} \frac{\Delta s\text{O}_2}{\Delta s\text{O}_2_{\text{max}}} &= \frac{(s\text{O}_2)_t - (s\text{O}_2)_{\text{base}}}{(s\text{O}_2)_{\text{max}} - (s\text{O}_2)_{\text{base}}} \\ &= \frac{\left(\frac{[\text{HbO}_2]_t}{[\text{Hb}_{\text{total}}]_t} - \frac{[\text{HbO}_2]_{\text{base}}}{[\text{Hb}_{\text{total}}]_{\text{base}}}\right)}{\left(\frac{[\text{HbO}_2]_{\text{max}}}{[\text{Hb}_{\text{total}}]_{\text{max}}} - \frac{[\text{HbO}_2]_{\text{base}}}{[\text{Hb}_{\text{total}}]_{\text{base}}}\right)}. \end{aligned} \quad (19)$$

During a cycle of oxygenation and deoxygenation in a blood-perfused tissue, if the total concentration of hemoglobin remains constant, we have the following condition: $[\text{Hb}_{\text{total}}]_{\text{max}} = [\text{Hb}_{\text{total}}]_t = [\text{Hb}_{\text{total}}]_{\text{base}}$. In the case of tumors under gas intervention, total hemoglobin concentration does not always remain constant, but the changes in $[\text{Hb}]_{\text{total}}$ appeared relatively small in comparison to the changes in $[\text{HbO}_2]$.^{11,18} It is reasonable to assume that $\Delta[\text{Hb}_{\text{total}}] \ll [\text{Hb}_{\text{total}}]$, i.e., the condition of $[\text{Hb}_{\text{total}}]_{\text{max}} = [\text{Hb}_{\text{total}}]_t = [\text{Hb}_{\text{total}}]_{\text{base}}$ still holds for the tumor under oxygen/carbogen interventions. Then, Eq. (19) becomes

$$\frac{\Delta sO_2}{\Delta sO_{2\max}} = \frac{(sO_2)_t - (sO_2)_{\text{base}}}{(sO_2)_{\max} - (sO_2)_{\text{base}}} = \frac{\Delta[\text{HbO}_2]}{\Delta[\text{HbO}_2]_{\max}} \quad (20)$$

To further make correlation between the normalized $\Delta[\text{HbO}_2]$ and blood pO_2 , Hill's equation¹⁹ can be combined with Eq. (20) to characterize oxygen transport in the tissue vasculature:

$$\begin{aligned} \frac{\Delta[\text{HbO}_2]}{\Delta[\text{HbO}_2]_{\max}} &= \frac{(pO_2^n) - (pO_2^n)_{\text{base}}}{(P_{50}^n) + (pO_2^n) - (sO_2)_{\text{base}}} \\ &= \frac{(pO_2^n) - b}{(P_{50}^n) + (pO_2^n) - a} \end{aligned} \quad (21)$$

where pO_2^B is the oxygen partial pressure in blood, P_{50}^B is the oxygen partial pressure in blood at $sO_2 = 50\%$, n is the Hill coefficient, $a = (sO_2)_{\max}$, and $b = (sO_2)_{\text{base}}$. This equation associates the normalized $\Delta[\text{HbO}_2]$ to blood pO_2 in tissues. It indicates that normalized $\Delta[\text{HbO}_2]$ measured from tissues/tumors under gas interventions is associated with normalized sO_2 between $(sO_2)_{\text{base}}$ and $(sO_2)_{\max}$ of the tissue/tumor, and it predicts the relationship between the normalized $\Delta[\text{HbO}_2]$ and blood pO_2 values in the tissue/tumor vasculature.

In our phantom studies, the measured pO_2 values are considered as blood pO_2 in tissue vasculature since blood is well mixed in the solution (see details in Sec. 3.4). Therefore, values of P_{50}^B , n , a , and b in Eq. (21) can be fitted to the experimental data, allowing us to determine the initial, transient, and maximal values of sO_2 of the simulating tissue due to oxygen/nitrogen interventions.

2.3 Relationship Between Normalized $\Delta[\text{HbO}_2]$ and Tissue/Tumor pO_2

In principle, blood pO_2 and tissue pO_2 are different, depending on the relative distance between a capillary vessel, oxygen consumption, and the location where pO_2 is measured.¹⁹ It is shown that there exists a constant pressure drop between blood pO_2 and tissue pO_2 as the blood passes through a capillary vessel. Therefore, it is reasonable to assume

$$pO_2^B = \alpha \cdot pO_2^T, \quad (22)$$

where pO_2^B and pO_2^T are blood pO_2 and tissue pO_2 values, respectively, and α is a constant representing an oxygen partial pressure drop from blood pO_2 to a local tissue pO_2 . Substituting Eq. (22) in Eq. (21) results in

$$\frac{\Delta[\text{HbO}_2]}{\Delta[\text{HbO}_2]_{\max}} = \frac{(pO_2^T)^n - b}{(P_{50}^n) + (pO_2^T)^n - a}, \quad (23)$$

where P_{50}^T is the oxygen partial pressure in tissue resulting from P_{50}^B , and the meanings of n , a , and b remain the same as in Eq. (21). This equation shows how normalized $\Delta[\text{HbO}_2]$ measured from tissue under gas interventions is associated with both tissue pO_2 and normalized sO_2 between $(sO_2)_{\text{base}}$ and $(sO_2)_{\max}$ in the tissue vasculature.

Ideally, when both $\Delta[\text{HbO}_2]$ and tissue pO_2 are measured at the same physical location, the maximal and initial oxygen saturations, i.e., a and b in Eq. (23), of the measured tissue vasculature can be obtained by fitting Eq. (23) to the measured data. In our tumor study, we then can estimate the maximal and initial hemoglobin oxygen saturations of the tumor by fitting the measured values of global normalized $\Delta[\text{HbO}_2]$ and global tissue pO_2 , which result from adding up all local pO_2 values obtained from ^{19}F MR pO_2 mapping.

3 Materials and Methods

3.1 Tumor Model

Dunning prostate rat tumors (eight R3327-HI and four R3327-AT1)²⁰ were implanted in pedicles on the foreback of adult male Copenhagen rats, as described in detail previously.²¹ Once the tumors reached approximately 1 cm in diameter, the rats were anesthetized with 0.2 ml ketamine hydrochloride (100 mg/mL; Aveco, Fort Dodge, IA) and maintained under general gaseous anesthesia with isoflurane in air (1.3% isoflurane at 1 dm³/min air) through a mask placed over the mouth and nose. Tumors were shaved to improve optical contact for transmitting light. Body temperature was maintained by a warm water blanket and was monitored by a rectally inserted thermal probe connected to a digital thermometer (Digi-Sense, model 91100-50, Cole-Parmer Instrument Company, Vernon Hills, IL). A pulse oximeter (model 8600, Nonin, Inc., Plymouth, MN) was placed on the hind foot to monitor arterial oxygenation (S_aO_2). Tumor volume V (in cubic centimeters) was estimated as $V = (4\pi/3) [(L+W+H)/6]^3$, where L , W , and H are the three respective orthogonal dimensions.

In general, the source-detector fiber separation was about 1 to 1.5 cm in transmittance geometry, and thus the maximal tumor volume interrogated by NIR light can be estimated as follows. By the diffusion approximation, the optical penetration depth from the central line between the source and detector is about one half of the separation (source-detector separation = d). The total tumor volume interrogated by NIR light can be estimated as the spherical volume with a radius of one half of d , i.e., $(\pi/6)d^3$. In this way, the estimated tumor volume interrogated by NIR light is in the range of 0.5 to 2.0 cm³, depending on the actual source-detector separation.

3.2 NIRS and pO_2 Needle Electrode Measurements

Figure 1 shows the schematic setup for animal experiments using both NIRS and a pO_2 needle electrode. A needle type oxygen electrode was placed in the tumor, and the reference electrode was placed rectally. The electrodes were connected to a picoammeter (Chemical Microsensor, Diamond Electro-Tech Inc., Ann Arbor, MI) and polarized at -0.75 V. Linear two-point calibrations were performed with air (21% O_2) and pure nitrogen (0% O_2) saturated saline buffer solutions before the electrode was inserted into the tumor, and we estimated an instrumental precision of 2 to 3 mm Hg. Measurement points of pO_2 were manually recorded, while the NIRS data were acquired automatically. Measurements of pO_2 and NIRS were initiated, while the rats breathed air for ~ 10 min to demonstrate a stable baseline. The inhaled gas was then switched to carbogen for 15 min and switched back to air.

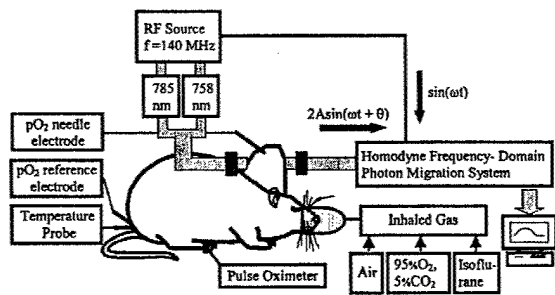


Fig. 1 Schematic experimental setup of one-channel, near-infrared, frequency-domain IQ instrument for tumor investigation *in vivo*. The 5-mm-diameter fiber bundles deliver the laser light, comprising two wavelengths (758 and 785 nm), and detect the laser light transmitted through the implanted tumor. The pO_2 needle electrode measures tumor tissue pO_2 .

Our NIR system as shown in Figure 1 (Refs. 11 and 22) is a homodyne frequency-domain photon migration system (NIM, Inc., Philadelphia, PA) and uses commercially available in-phase and quadrature (IQ) demodulator chips to demodulate the detected, amplitude-modulated optical signal.

3.3 Experimental Validation for β_{HbO_2} and β_{Hb} Values

In order to validate β_{HbO_2} and β_{Hb} values, we conducted phantom calibration measurements. We used 2 l of 0.01 M phosphate buffered saline (P-3813, Sigma, St Louis, MO) and 1% Intralipid (Intralipid® 20%, Baxter Healthcare Corp., Deerfield, IL) with pH=7.4 at 25 °C. To deoxygenate the solution, 14 g of baking yeast was dissolved in the phantom solution, and pure oxygen gas was used to oxygenate the solution. After the yeast was well mixed in the solution, 3 ml of human blood was added twice. When the blood was fully deoxygenated, pure oxygen was introduced in the solution to oxygenate the blood. After the blood was fully oxygenated, oxygen blowing was stopped in order to deoxygenate the solution with yeast again.

Equations (4) and (5) were applied to the raw amplitude data to calculate $\Delta[HbO_2]$ and $\Delta[Hb]$. Large unexpected and erroneous fluctuation of $\Delta[Hb]_{total}$ ($=\Delta[HbO_2]+\Delta[Hb]$) were seen during the oxygenation and deoxygenation cycles (Figure 2). However, when we applied Eqs. (13) to (15) to calculate $\Delta[HbO_2]$, $\Delta[Hb]$, and $\Delta[Hb]_{total}$, $\Delta[Hb]_{total}$ remained constant during the oxygenation and deoxygenation cycles as expected. This demonstrates that the values of $\beta_{HbO_2}=1.103$ and $\beta_{Hb}=0.9035$ are correct and necessary to compensate the differences in DPFs caused by the two different wavelengths.

3.4 Tissue Phantom Solution Model

In order to study the relationship between pO_2 and $\Delta[HbO_2]$ in regular tissues, we conducted a tissue-simulating phantom study by using the liquid solution similar to that mentioned above. In normal tissues, there are several steps of oxygen transport from the blood to tissue cells.²³ In the tissue-simulating phantom, blowing oxygen gas represents oxygenation process of blood in the lungs, and blowing nitrogen gas simulates deoxygenation process of blood in the tissues. The

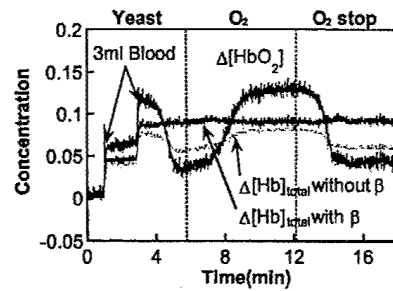


Fig. 2 Simultaneous dynamic changes of $\Delta[HbO_2]$, $\Delta[Hb]$, and $\Delta[Hb]_{total}$ in the phantom solution measured using NIRS. The gray solid curve is for $\Delta[Hb]_{total}$ without using β_{HbO_2} and β_{Hb} values. Oxygen consumption by yeast produced deoxygenated blood and blowing oxygen restored oxygenation. During the oxy- and deoxygenation process, $\Delta[Hb]_{total}$ is supposed to be a constant. However, as we can see here, $\Delta[Hb]_{total}$ calculated without β_{HbO_2} and β_{Hb} values shows the fluctuation during the oxy- and deoxygenation while $\Delta[Hb]_{total}$ calculated using β_{HbO_2} and β_{Hb} values shows the veracity of these modified algorithms.

differences between the tissue-simulating phantom and real tissues are that there is no capillary membrane in the phantom, and that the phantom is more homogeneous than real tissues. Capillary membranes have high permeability of oxygen, so oxygen transport from blood to tissues crossing the capillary membranes occurs straightforwardly. Furthermore, normal tissues are well vascularized, and the NIR techniques are more sensitive toward measuring small vessels and vascular bed of the tissue.²⁴ Therefore, vasculature of normal tissues has been simulated by a turbid solution mixed with blood as a simplified laboratory model in NIRS measurements for oxygen transport from blood to normal tissues.^{10,18,22}

The experimental setup shown in Figure 3 was made to simulate tumor oxygenation/deoxygenation. Oxygen needle electrodes, a pH electrode, and a thermocouple probe (model 2001, Sentron, Inc., Gig Harbor, WA) were placed in the solution, and the gas tube for delivery of N_2 or air was placed opposite the NIRS probes to minimize any liquid movement effects. Source and detector probes for the NIRS were placed in reflection geometry with a direct separation of 3 cm. The

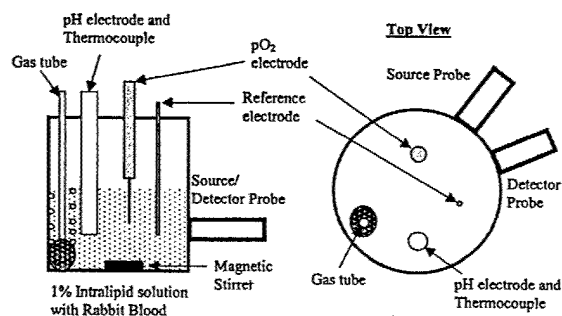


Fig. 3 Experimental setup for phantom study using 1% Intralipid in saline buffer. NIRS probes were placed in reflectance mode, while the gas bubbler was placed opposite to minimize liquid movement effects. After adding 2 ml of rabbit blood to a 200 ml solution, nitrogen gas and air were introduced to deoxygenate and oxygenate the solution, respectively.

solution was stirred constantly to maintain homogeneity by a magnetic stirrer at $\sim 37^\circ\text{C}$. Fresh whole rabbit blood (2 mL) was added to the 200 mL solution before baseline measurement. Nitrogen gas and air were used to deoxygenate and oxygenate the solution, respectively.

3.5 MRI Instrumentation and Procedure

To support the findings obtained from the $p\text{O}_2$ electrode measurements and NIRS, we conducted MRI experiments using an Omega CSI 4.7 T 40 cm system with actively shielded gradients. A homebuilt tunable $^1\text{H}/^{19}\text{F}$ single turn solenoid coil was placed around the tumor. 45 μL hexafluorobenzene (HFB; Lancaster, Gainesville, FL) was administered directly into the tumor using a Hamilton syringe (Reno, NV) with a custom-made fine sharp (32 gauge) needle and HFB was deliberated dispersal along several tracks to interrogate both central and peripheral tumor regions, as described in detail previously.⁵ HFB is ideal for imaging $p\text{O}_2$ because it has a single resonance and its relaxation rate varies linearly with oxygen concentration. ^1H images were acquired for anatomical reference using a traditional 3-D spin-echo pulse sequence. Conventional ^{19}F MR images were taken to show the 3-D distribution of the HFB in the tumor. ^{19}F MR images were directly overlaid over ^1H images to show the position of the HFB in that slice.

Tumor oxygenation was assessed using fluorocarbon relaxometry using echo planar imaging for dynamic oxygen mapping (FREDOM) based on ^{19}F pulse burst saturation recovery (PBSR) echo planar imaging (EPI) of HFB.²⁵ The PBSR preparation pulse sequence consists of a series of 20 nonspatially selective saturating 90 deg pulses with 20 ms spacing to saturate the ^{19}F nuclei. Following a variable delay time τ , a single spin-echo EPI sequence with blipped phase encoding was applied.²⁶ Fourteen 32×32 PBSR-EPI images, with τ ranging from 200 ms to 90 sec and a field of view (FOV) of 40×40 mm, were acquired in 8 min using the alternated relaxation delays with variable acquisitions to reduce clearance effects (ARDVARC) acquisition protocol.²⁵ An $R1 (=1/T1)$ map was obtained by fitting the signal intensity of each voxel of the 14 images to a three-parameter relaxation model by the Levenberg-Marquardt least-squares algorithm:

$$y_n(i,j) = A(i,j) \cdot [1 - (1+W)\exp(-R1(i,j) \cdot \tau_n)] \quad (24)$$

$$(n=1,2,\dots,14)$$

$$(i,j=1,2,\dots,32),$$

where $y_n(i,j)$ is the measured signal intensity corresponding to delay time τ_n (the n 'th images) for voxel (i,j) , $A(i,j)$ is the fully relaxed signal intensity amplitude of voxel (i,j) , W is a dimensionless scaling factor allowing for imperfect signal conversion, $R1(i,j)$ is the relaxation rate of voxel (i,j) in units of sec^{-1} , and A , W , and $R1$ are the three fit parameters for each of the 32×32 voxels. Finally, the $p\text{O}_2$ maps were generated by applying the calibration curve, $p\text{O}_2$ (mm Hg) $= [R1(\text{s}^{-1}) - 0.0835]/0.001876$ at 37°C , to the $R1$ maps.²⁵

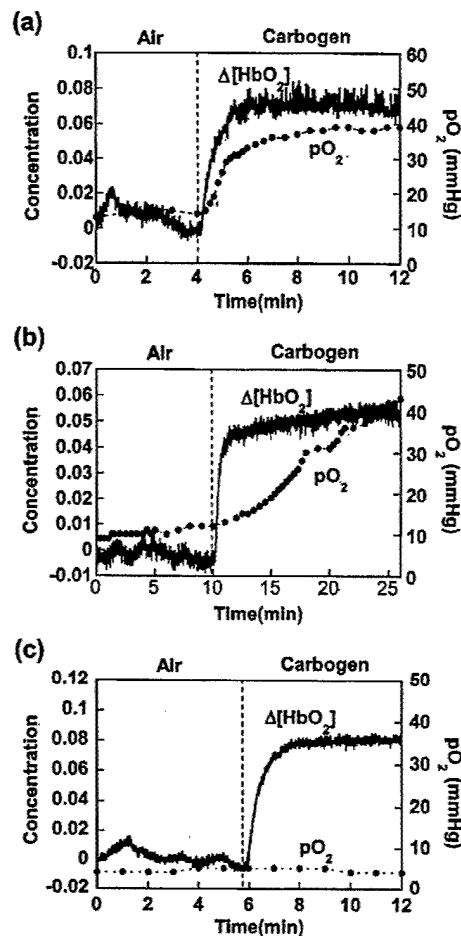


Fig. 4 Simultaneous dynamic changes of $\Delta[\text{HbO}_2]$ and $p\text{O}_2$ in R3327-HI rat prostate tumors using NIRS and $p\text{O}_2$ needle electrode. (a) A small tumor (1.5 cm^3) showed a rapid $p\text{O}_2$ response (case 1), whereas (b) a bigger tumor (3.1 cm^3) showed a slower $p\text{O}_2$ response (case 2). (c) In a third tumor (1.6 cm^3) where regional baseline $p\text{O}_2$ was $< 5 \text{ mm Hg}$, there was no $p\text{O}_2$ response (case 3). The unit of $\Delta[\text{HbO}_2]$ is mM/DPF , where DPF is equal to the optical path length divided by the source-detector separation. Dotted vertical line marks the time when the gas was changed.

4 Results

4.1 Tumor Study Results

We have measured relative changes of $[\text{HbO}_2]$, $[\text{Hb}]$, $[\text{Hb}_{\text{total}}]$, and tumor tissue $p\text{O}_2$ (electrode) from eight Dunning prostate R3327-HI tumors, and Figure 4 shows three representative data sets. Figure 4(a) shows the temporal profiles of $\Delta[\text{HbO}_2]$ and $p\text{O}_2$ in a small Dunning prostate R3327-HI tumor (1.5 cm^3) measured simultaneously with NIRS and the $p\text{O}_2$ needle electrode during respiratory challenge. After a switch from air to carbogen, $\Delta[\text{HbO}_2]$ increased rapidly, along with tumor tissue $p\text{O}_2$. Figure 4(b) was obtained from a large tumor (3.1 cm^3): the electrode readings showed a slower $p\text{O}_2$ response, whereas the NIRS response was biphasic, which has been a commonly observed dynamic feature.¹¹ In a third tumor (1.6 cm^3), NIRS behaved as before, but $p\text{O}_2$ did not change [Figure 4(c)].

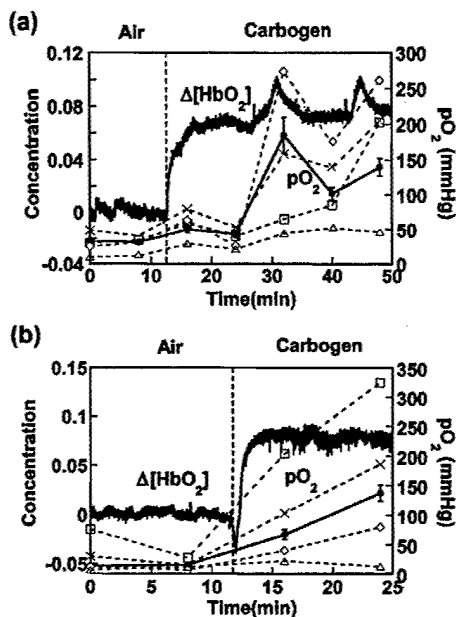


Fig. 5 Dynamic changes of $\Delta[\text{HbO}_2]$ and $p\text{O}_2$ in two R3327-AT1 rat prostate tumors measured sequentially using NIRS and ^{19}F MR $p\text{O}_2$ mapping. The solid curves represent $\Delta[\text{HbO}_2]$, and the solid lines with solid circles represent mean $p\text{O}_2 \pm \text{SE}$ (standard error) of 21 (a) and 45 (b) voxels of the respective tumor. Dashed lines with open symbols are 4 representative voxels for each case. After a gas switch from air to carbogen, the mean $p\text{O}_2$ values of both tumors increased, but individual voxels showed quite different responses, indicating high heterogeneity in the tumors. The tumor sizes were 3.2 cm^3 and 2.7 cm^3 for (a) and (b), respectively.

In four tumors from a separate subline (Dunning prostate R3327-AT1), NIRS and ^{19}F MRI were taken sequentially with carbogen challenge, and two representative data sets are shown in Figure 5. NIRS response showed vascular oxygenation changes as before, and FREDOM revealed the distinct heterogeneity of the tumor tissue response. Initial $p\text{O}_2$ was in the range of 1 to 75 mm Hg, and carbogen challenge produced $p\text{O}_2$ values in the range of 6 to 350 mm Hg. Representative voxels are shown in each figure by dashed lines with open symbols. In addition, mean $p\text{O}_2$ values were calculated by averaging all available $p\text{O}_2$ readings over 21 and 45 voxels for the two respective tumors. We usually obtain $p\text{O}_2$ temporal profiles from individual voxels among 200 to 400 voxels in a tumor during the entire intervention period. The $p\text{O}_2$ readings presented here were picked to show heterogeneity of the tumor. In Figure 5(a), the closest distance between the two voxels is 1.25 mm (between \diamond and \square), and the furthest distance is 7.6 mm (between \times and Δ). In Figure 5(b), the closest distance is 3.6 mm (between \times and Δ) and the furthest distance is 16 mm (between \times and \square). These indeed showed that tumor $p\text{O}_2$ responses to carbogen intervention could be quite different at different locations. Notice that Figure 5(a) showed spikes of $\Delta[\text{HbO}_2]$ during the measurement. We expect this to be caused by sudden changes in rat respiratory circulation or motion, rather than resulting from simple instrumental noise. It is also seen that mean $p\text{O}_2$ values have displayed a consistent increase when $\Delta[\text{HbO}_2]$ showed

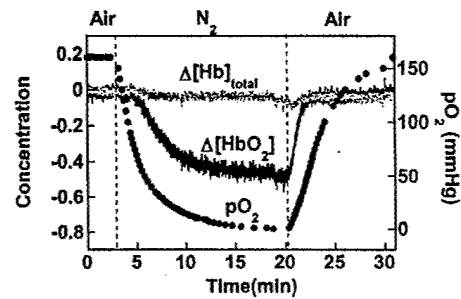


Fig. 6 Simultaneous dynamic changes of $\Delta[\text{HbO}_2]$, $\Delta[\text{Hb}]_{\text{total}}$, and $p\text{O}_2$ in the phantom solution measured using NIRS and $p\text{O}_2$ needle electrode. The dark solid curve is for $\Delta[\text{HbO}_2]$, the lighter solid line is for $\Delta[\text{Hb}]_{\text{total}}$, and the solid circles show $p\text{O}_2$ values in the phantom solution. After ~ 3 min baseline, the bubbling gas was changed from air to nitrogen to deoxygenate the solution and then switched back to air to reoxygenate the solution. The unit of $\Delta[\text{HbO}_2]$ is mM/DPF.

spikes, suggesting that such spikes may result from changes in rat physiological conditions.

4.2 Tissue Phantom Study Results

Figure 6 shows a temporal profile for $\Delta[\text{HbO}_2]$ and $p\text{O}_2$ measured from the tissue phantom during a cycle of gas change from air to nitrogen and back. The first three minutes were measured as a baseline after adding 2 ml blood. Bubbling nitrogen deoxygenated the solution and caused the $p\text{O}_2$ values to fall; $\Delta[\text{HbO}_2]$ declined accordingly with a small time lag. After the bubbling gas was switched from nitrogen to air, both $\Delta[\text{HbO}_2]$ and $p\text{O}_2$ started to increase simultaneously, but the recovery time of $\Delta[\text{HbO}_2]$ to the baseline was faster than that of $p\text{O}_2$. The small time lag between the changes of $\Delta[\text{HbO}_2]$ and $p\text{O}_2$ is probably due to the allosteric interactions between hemoglobin and oxygen molecules. According to the hemoglobin oxygen-dissociation curve,^{19,27} oxyhemoglobin starts to lose oxygen significantly when $p\text{O}_2$ falls below 70 mm Hg at standard conditions ($\text{pH}=7.4$, $p\text{CO}_2=40$ mm Hg, and temperature $=37^\circ\text{C}$). The same principle can explain why $\Delta[\text{HbO}_2]$ has a faster recovery than that of $p\text{O}_2$. Figure 6 shows that $\Delta[\text{HbO}_2]$ is already saturated when $p\text{O}_2$ is at 50 mm Hg, while the solution was still being oxygenated. This may be due to low $p\text{CO}_2$ in the solution where this can shift the oxyhemoglobin dissociation curve to the left, causing oxyhemoglobin to be saturated at lower $p\text{O}_2$. Importantly, $\Delta[\text{Hb}]_{\text{total}}$ remained unchanged, as expected, during a cycle of deoxygenation and oxygenation.

4.3 Correlation between $p\text{O}_2$ and Normalized $\Delta[\text{HbO}_2]$

For Tissue Phantoms. Figure 7(a) replots the data given in Figure 6, showing the relationship between normalized $\Delta[\text{HbO}_2]$ and $p\text{O}_2$ measured from the tissue phantom during the oxygenation (air blowing) period after the nitrogen blowing. Open circles are the measured data, and the solid line is the fitted curve using Eq. (23). The error bars for the data were not shown here since they are smaller than the symbols of the data points. For the curve fitting procedure, we used a nonlinear curve-fitting routine provided through Kaleidagraph (Synergy software, Reading, PA). The fitted parameters

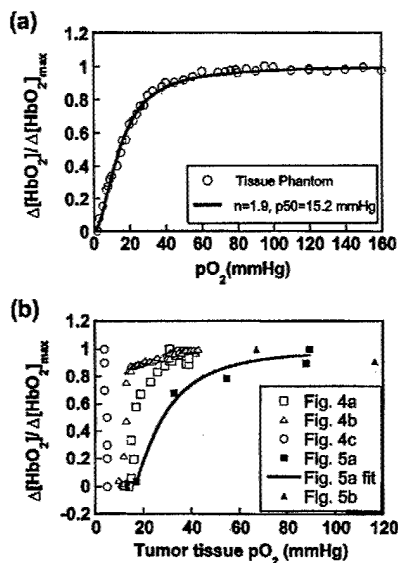


Fig. 7 Changes of tissue pO_2 with normalized changes of oxygenated hemoglobin (a) in the phantom solution using the NIRS and pO_2 needle electrode, and (b) in tumors measured with NIRS, pO_2 needle electrode, and ^{19}F MR pO_2 mapping. In (a), the open circles are measured data and the solid line is the fitted curve using Eq. (21). This shows that Eq. (21) works well in a homogeneous system. In (b), all the tumor data are shown indicating that tumors are highly heterogeneous for pO_2 response to carbogen inhalation. Open symbols show local pO_2 changes (from Figure 4) and solid symbols show the mean pO_2 changes (from Figure 5) during gas intervention. To estimate global sO_2 in tumors during respiratory challenges, we applied Eq. (23) to Figure 5(a), indicating sO_2 changes during carbogen inhalation when compared via tumor pO_2 .

are $n=1.9$, $P_{50}=15.2 \text{ mmHg}$, $[\text{sO}_2]_{\text{base}}=0\%$, and $[\text{sO}_2]_{\text{max}}=99\%$ with $R=0.997$ and minimized chi-square. The fitted values of $[\text{sO}_2]_{\text{base}}$ and $[\text{sO}_2]_{\text{max}}$ are in good agreement with the expected values, since the corresponding pO_2 values are 0 and 160 mm Hg, respectively. This agreement validates Eq. (23) and further indicates that we can measure approximate sO_2 values during the gas interventions in a homogeneous system by fitting the experimental data using Eq. (23) even though we do not measure absolute $[\text{HbO}_2]$. The Hill coefficient (n) and pO_2 value at 50% of sO_2 (P_{50}) are smaller than the values from a standard oxyhemoglobin saturation curve, probably due to the shift of the oxyhemoglobin dissociation curve.

For Tumor Study. Figure 7(b) replots the data given in Figures 4 and 5, showing a direct relationship between the normalized $\Delta[\text{HbO}_2]$ and tissue pO_2 in the tumors. NIRS results tended to be similar for several tumors, and pO_2 electrode measurements showed considerable variation even in the same tumor type, suggesting distinct tumor heterogeneity. This was substantiated by the ^{19}F MR pO_2 mappings (Figure 5): indeed, in some cases, pO_2 values did not change with respiratory challenge, especially when baseline pO_2 values were lower than 10 mm Hg.

Equation (23) can be used to estimate values of $[\text{sO}_2]_{\text{base}}$ and $[\text{sO}_2]_{\text{max}}$ for the tissue-simulating phantom (a homogeneous system). However, the relationship fails for heteroge-

neous systems such as tumors. The NIRS measurements interrogate a large volume of tumor tissue, giving a global value of normalized $\Delta[\text{HbO}_2]$, whereas the pO_2 readings are local near the tip of the needle electrode. However, to estimate mean values of $[\text{sO}_2]_{\text{base}}$ and $[\text{sO}_2]_{\text{max}}$, it is reasonable to compare the global normalized $\Delta[\text{HbO}_2]$ with global tissue pO_2 , which can be obtained by summing up all local pO_2 readings at different pixels measured from the ^{19}F MRI mapping, as done in Sec. 4.1 and shown by solid lines in Figure 5. The data shown in Figure 7(b) with solid symbols are the global mean pO_2 values calculated from the corresponding MRI data. The solid fitting curve shown in Figure 7(a) is obtained from the mean pO_2 data given in Figure 5(a). In this case, the fitting parameters are P_{50} , $[\text{sO}_2]_{\text{base}}$, and $[\text{sO}_2]_{\text{max}}$ with a fixed Hill coefficient n to be the same as that under standard conditions. The best fitting curve of Eq. (23) is shown in Figure 7(b), having $P_{50}=20.6 \pm 4.1 \text{ mmHg}$, $[\text{sO}_2]_{\text{base}}=37 \pm 13\%$, and $[\text{sO}_2]_{\text{max}}=100\%$ with $R=0.985$ and goodness-of-fit $\chi^2=0.031$. Estimated errors for P_{50} and $[\text{sO}_2]_{\text{base}}$ are not insignificant and a better fit could be found by measuring pO_2 with better temporal resolution.

5 Discussion and Conclusion

Tumor oxygenation involves a complex interplay of multiple compartments and parameters: blood flow, blood volume, blood vessel structure, and oxygen consumption. NIRS provides a global noninvasive estimate of average vascular oxygenation encompassing arterial, venous, and capillary compartments. In agreement with our previous observations,¹¹ the $\Delta[\text{HbO}_2]$ response is often biphasic, which we believe represents rapid elevation of arterial oxygenation, followed by more sluggish capillary components.

Comparison with simultaneous electrode measurements indeed revealed that tumors are heterogeneous. Like NIRS measurements, pO_2 electrodes provide rapid assessment of pO_2 facilitating real-time observation of dynamic changes. In Figure 4(a), pO_2 starts at a baseline value $\sim 15 \text{ mmHg}$ and increases rapidly in response to respiratory challenge with carbogen. Indeed, the rate approaches that of the vascular compartments. In a second tumor [Figure 4(b)], where the interrogated location showed a slightly lower pO_2 , the tissue response was more sluggish. For a third HI tumor, local baseline pO_2 was found to be $< 5 \text{ mmHg}$, and this did not change with carbogen inhalation despite the response observed by NIRS. This suggests a danger of comparing a global vascular measurement with regional tumor pO_2 , since tumors are known to be highly heterogeneous. This also demonstrates an essential need for NIR imaging of tumors to provide regional tumor vascular oxygenation details.

FREDOM measurements in Figure 5 revealed the heterogeneity in baseline oxygenation within individual tumors of this second tumor subline as also reported previously.²⁵ Baseline pO_2 ranged from 1 to 75 mm Hg, and response to carbogen was variable in terms of rate and extent, as also seen for the HI subline using electrodes (Figure 4). As with the electrodes, the better oxygenated tumor regions showed a faster and greater response to carbogen inhalation. The oxygen electrode measurements in Figure 4 showed a maximum pO_2 of around 45 mm Hg, though we have observed values as high as 95 mm Hg using oxygen needle electrode. Observations using

the fluorescence-based OxyLite™ fiber-optic devices for measuring HI tumor reached the maximum detectable pO_2 of 100 mm Hg during carbogen inhalation.⁵ FREDOM has shown values of less than 5 mm Hg and greater than 160 mm Hg under air breathing conditions, and reaching 350 mm Hg in HI tumors while breathing carbogen.⁵ Each method indicates that tumors are highly heterogeneous, but it has been shown that there can be a positive linear relationship between baseline pO_2 and maximum pO_2 during carbogen inhalation in the Dunning prostate AT1 tumor line.⁸

The phantom measurements indicate and validate the reliability of the NIRS technique and also prove that normalized $\Delta[HbO_2]$ is closely related to the normalized hemoglobin-oxygen dissociation curve. The phantom data confirmed that we can obtain absolute sO_2 values in a homogeneous system by measuring both $\Delta[HbO_2]$ and pO_2 . We could estimate mean sO_2 values of the tumor under intervention using global $\Delta[HbO_2]$ and averaged pO_2 readings, and the fitting errors are expected to be improved by having more data points. Measuring regional tumor vascular oxygenation by NIR imaging of tumors should allow us to correlate local $\Delta[HbO_2]$ and pO_2 and to understand the oxygen transport process from tumor vasculature to tumor tissue, and this is the direction of our future work.

Both NIRS and electrodes offer essentially real-time measurement of changes in oxygenation, which can be rapid (Figure 4). Indeed, the inflow kinetics of vascular O_2 detected by NIRS are similar to those previously reported in the HI tumor line following a bolus of the paramagnetic contrast agents Gd-DTPA.²⁸ FREDOM has lower temporal resolution, but reveals the tumor heterogeneity and differential response of regions exhibiting diverse baseline pO_2 . The results here correspond closely with more extensive observation.^{5,8,25} While FREDOM currently requires 6.5 min per pO_2 map, we have previously demonstrated an alternative data acquisition protocol achieving 1 s time resolution in a perfused heart, albeit providing less precision in measurements and only a global determination.²⁹ Such an approach could allow us to measure global $\Delta[HbO_2]$ and global pO_2 simultaneously with a high temporal resolution, understand the relationship between global $\Delta[HbO_2]$ and global pO_2 , and obtain absolute values of sO_2 of the tumors as tumors grow.

In conclusion, we have refined the algorithms for calculating $[Hb]$, $[HbO_2]$, and $[Hb_{total}]$ and measured relative $[HbO_2]$ changes in tumor vasculature and tumor tissue pO_2 under carbogen intervention using NIRS and a needle type pO_2 electrode. The pO_2 data were also supported by the ^{19}F MR pO_2 mapping. We have also developed an algorithm to estimate sO_2 values in the tumor during respiratory interventions. The NIRS data showed significant changes in vascular oxygenation accompanying respiratory interventions, and changes in tumor vascular oxygenation preceded tumor tissue pO_2 . Oxygen electrode measurements and ^{19}F MR pO_2 mapping results proved that tumors are highly heterogeneous. The phantom data confirmed that normalized $[HbO_2]$ data together with pO_2 measurements can be used to estimate absolute sO_2 values in a homogeneous system. For a highly heterogeneous medium, such as tumors, local comparison between the $[HbO_2]$ and pO_2 value is desired and required in order to reveal the process of oxygen delivery from the tumor

vascular bed to the tumor tissues. Therefore, this study not only demonstrates that the NIRS technology can provide an efficient, real-time, noninvasive approach to monitoring tumor physiology and is complementary to other techniques, but also emphasizes the need to develop an imaging technique to study spatial heterogeneity of tumor vasculature under oxygen or other therapeutic interventions.

Acknowledgments

This work was supported in part by the Department of Defense Breast Cancer Initiative grant BC990287 (HL) and NIH RO1 CA79515 (RPM). NMR experiments were conducted at the Mary Nell & Ralph B. Rogers MR Center, an NIH BRTP Facility no. 5-P41-RR02584. We are grateful to Dr. Britton Chance from the University of Pennsylvania for assistance with tissue phantom study and to Dr. Peter Peschke for providing the original tumor cells.

References

1. L. Gray, A. Conger, M. Ebert, S. Hornsey, and O. Scott, "The concentration of oxygen dissolved in tissues at time of irradiation as a factor in radio-therapy," *Br. J. Radiol.* **26**, 638–648 (1953).
2. J. H. Kaanders, L. A. Pop, H. A. Marres, J. Liefers, F. J. van den Hoogen, W. A. van Daal, and A. J. van der Kogel, "Accelerated radiotherapy with carbogen and nicotinamide (ARCON) for laryngeal cancer," *Radiother. Oncol.* **48**, 115–122 (1998).
3. J. Overgaard and M. R. Horsman, "Modification of hypoxia-induced radioresistance in tumors by the use of oxygen and sensitizers," *Semin. Radiat. Oncol.* **6**, 10–21 (1996).
4. H. B. Stone, J. M. Brown, and T. Phillips, "Oxygen in human tumors: correlations between methods of measurement and response to therapy," *Radiat. Res.* **136**, 422–434 (1993).
5. D. Zhao, A. Constantinescu, E. W. Hahn, and R. P. Mason, "Tumor oxygenation dynamics with respect to growth and respiratory challenge: investigation of the Dunning prostate R3327-HI tumor," *Radiat. Res.* **156**(5), 510–520 (2001).
6. D. Cater and I. Silver, "Quantitative measurements of oxygen tension in normal tissues and in the tumors of patients before and after radiotherapy," *Acta Radiol. (1921-1962)* **53**, 233–256 (1960).
7. J. A. O'Hara, F. Goda, E. Demidenko, and H. M. Swartz, "Effect on regrowth delay in a murine tumor of scheduling split-dose irradiation based on direct pO_2 measurements by electron paramagnetic resonance oximetry," *Radiat. Res.* **150**, 549–556 (1998).
8. R. P. Mason, A. Constantinescu, S. Hunjan, D. Le, E. W. Hahn, P. P. Antich, C. Blum, and P. Peschke, "Regional tumor oxygenation and measurement of dynamic changes," *Radiat. Res.* **152**, 239–249 (1999).
9. M. S. Patterson, B. Chance, and B. C. Wilson, "Time resolved reflectance and transmittance for the non-invasive measurement of tissue optical properties," *Appl. Opt.* **28**, 2331–2336 (1986).
10. E. M. Sevick, B. Chance, J. Leigh, S. Nokia, and M. Maris, "Quantitation of time- and frequency-resolved optical spectra for the determination of tissue oxygenation," *Anal. Biochem.* **195**, 330–351 (1991).
11. H. Liu, Y. Song, K. L. Worden, X. Jiang, A. Constantinescu, and R. P. Mason, "Noninvasive investigation of blood oxygenation dynamics of tumors by near-infrared spectroscopy," *Appl. Opt.* **39**, 5231–5243 (2000).
12. W. G. Zijlstra, A. Buursma, and W. P. Meeuwse-van der Roest, "Absorption spectra of human fetal and adult oxyhemoglobin, deoxyhemoglobin, carboxyhemoglobin, and methemoglobin," *Clin. Chem.* **37**, 1633–1638 (1991).
13. D. T. Delpy, M. Cope, P. van der Zee, S. Arridge, S. Wray, and J. Wyatt, "Estimation of optical pathlength through tissue from direct time of flight measurement," *Phys. Med. Biol.* **33**(12), 1433–1442 (1988).
14. M. Ferrari, Q. Wei, L. Carrarresi, R. A. De Blasi, and G. Zaccanti, "Time-resolved spectroscopy of human forearm," *J. Photochem. Photobiol.* **16**, 141–153 (1992).
15. P. van der Zee, M. Cope, S. R. Arridge, M. Essenpreis, L. A. Potter,

- A. D. Edwards, J. S. Wyatt, D. C. McCormick, S. C. Roth, E. O. R. Reynolds, and D. T. Delpy, "Experimentally measured optical path-lengths for the adult head, calf and forearm and the head of the newborn infants as a function of inter optode spacing," *Adv. Exp. Med. Biol.* **316**, 143–153 (1992).
16. R. G. Steen, K. Kitagishi, and K. Morgan, "In vivo measurement of tumor blood oxygenation by near-infrared spectroscopy: immediate effects of pentobarbital overdose or carmustine treatment," *J. Neuro-Oncol.* **22**, 209–220 (1994).
17. H. Liu, "Unified analysis of the sensitivities of reflectance and path length to scattering variations in a diffusive medium," *Appl. Opt.* **40**(10), 1742–1746 (2001).
18. E. L. Hull, D. L. Conover, and T. H. Foster, "Carbogen-induced changes in rat mammary tumour oxygenation reported by near infrared spectroscopy," *British J. Cancer* **79**(11/12), 1709–1716 (1999).
19. R. L. Fournier, "Oxygen transport in biological systems," Chap. 4 in *Basic Transport Phenomena in Biomedical Engineering*, pp. 87–94, Taylor & Francis, Lillington (1999).
20. P. Peschke, E. W. Hahn, F. Lohr, F. Brauschweig, G. Wolber, I. Zuna, and M. Wannenmacher, "Differential sensitivity of three sublines of the rat Dunning prostate tumor system R3327 to radiation and/or local tumor hyperthermia," *Radiat. Res.* **150**, 423–430 (1998).
21. E. W. Hahn, P. Peschke, R. P. Mason, E. E. Babcock, and P. P. Antich, "Isolated tumor growth in a surgically formed skin pedicle in the rat: a new tumor model for NMR studies," *Magn. Reson. Imaging* **11**, 1007–1017 (1993).
22. Y. Yang, H. Liu, X. Li, and B. Chance, "Low-cost frequency-domain photon migration instrument for tissue spectroscopy, oximetry, and imaging," *Opt. Eng.* **36**, 1562–1569 (1997).
23. M. H. Friedman, "Gas transport," Chap. 9 in *Principles and Models of Biological Transport*, pp. 240–242, Springer, Berlin Heidelberg (1986).
24. H. Liu, A. H. Hielscher, F. K. Tittel, S. L. Jacques, and B. Chance, "Influence of blood vessels on the measurement of hemoglobin oxygenation as determined by time-resolved reflectance spectroscopy," *Med. Physics* **22**, 1209–1217 (1995).
25. S. Hunjan, D. Zhao, A. Constantinescu, E. W. Hahn, P. Antich, and R. P. Mason, "Tumor oximetry: demonstration of an enhanced dynamic mapping procedure using fluorine-19 echo planar magnetic resonance imaging in the dunning prostate R3327-AT1 rat tumor," *Int. J. Radiat. Oncol., Biol., Phys.* **49**, 1097–1108 (2001).
26. B. R. Barker, R. P. Mason, N. Bansal, and R. M. Peshock, "Oxygen tension mapping by ^{19}F echo planar NMR imaging of sequestered perfluorocarbon," *JMRI* **4**, 595–602 (1994).
27. S. I. Fox, "Respiratory physiology," Chap. 16 in *Human Physiology*, pp. 508–513, McGraw-Hill, Boston (1999).
28. G. Brix, J. Debus, M. Mueller-Schimpfle, P. Peschke, P. Huber, H. J. Zabel, and W. Lorenz, "MR-tomographische Quantifizierung struktureller und funktioneller Gewebeveränderungen an stosswellen-therapierten Dunning-Prostata-Tumoren," *Z. Med. Phys.* **3**, 76–82 (1993).
29. R. P. Mason, F. M. H. Jeffrey, C. R. Malloy, E. E. Babcock, and P. P. Antich, "A noninvasive assessment of myocardial oxygen tension: ^{19}F NMR spectroscopy of sequestered perfluorocarbon emulsion," *Magn. Reson. Med.* **27**, 310–317 (1992).